Available online at www.sciencedirect.com
ScienceDirect
Comput. Methods Appl. Mech. Engrg. 294 (2015) 449–485
Computer methods in applied mechanics and engineering
www.elsevier.com/locate/cma

Phase field modeling of fracture in multi-physics problems. Part I. Balance of crack surface and failure criteria for brittle crack propagation in thermo-elastic solids

Christian Miehe*, Lisa-Marie Schänzel, Heike Ulmer

Institute of Applied Mechanics (Civil Engineering), Chair I, University of Stuttgart, Pfaffenwaldring 7, 70569 Stuttgart, Germany

Available online 15 December 2014

Abstract

This work presents a generalization of recently developed continuum phase field models for brittle fracture towards fully coupled thermo-mechanical and multi-physics problems at large strains. It outlines a *rigorous geometric approach* to the diffusive crack modeling based on the introduction of a *balance of regularized crack surface*, governed by a crack phase field. The regularized crack surface functional is based on a crack surface density function, that describes the macroscopic crack surface in the bulk material per unit of the reference volume. The approach overcomes difficulties associated with the computational realization of sharp crack discontinuities, in particular when it comes to complex crack topologies. The formulation proposed is essentially a gradient damage theory, however, equipped with critical ingredients rooted in fracture mechanics. A *modular concept* is outlined for the linking of the diffusive crack modeling with complex multi-field response of the bulk material, where focus is put on the model problem of finite thermo-elasticity. This concerns a *generalization of crack driving forces* from the energetic definitions towards stress-based criteria, the constitutive modeling of heat conduction across cracks and convective heat exchanges at crack faces based on additional constitutive functions. This is achieved by approximating surface load integrals of the sharp crack approach by distinct volume integrals. We demonstrate the performance of the phase field formulation of fracture at large strains by means of representative numerical examples.

Keywords: Brittle fracture; Crack propagation; Phase field modeling; Finite strain; Coupled multi-field problems; Thermo-elasticity

1. Introduction

1.1. The phase field approach to brittle fracture

The prediction of failure mechanisms in solids due to crack initiation and propagation is of great importance for engineering applications. However, the computational modeling of *sharp* crack discontinuities suffers in situations

* Corresponding author. Tel.: +49 711 685 66379.
E-mail address: cm@mechbau.uni-stuttgart.de (C. Miehe).
URL: http://www.mechbau.uni-stuttgart.de/ls1/ (C. Miehe).

http://dx.doi.org/10.1016/j.cma.2014.11.016
0045-7825/

with complex crack topologies including branching. This can be overcome by a *diffusive* crack modeling based on the introduction of a crack phase field as proposed in Miehe et al. [1,2], Borden et al. [3,4], Verhoosel and de Borst [5]. These works outline thermodynamically consistent frameworks for the *continuum phase field modeling* of crack propagation that completely avoid the resolution of discontinuities. The formulations are essentially gradient damage theories, however, with critical ingredients rooted in fracture mechanics. This concerns in particular the introduction of a *crack surface density function* $\gamma_l(d, \nabla d)$, depending on a length scale l, which measures a spatially regularized total crack surface

$$\Gamma_l(d) = \int_{\mathcal{B}_0} \gamma_l(d, \nabla d)\, dV \tag{1}$$

with respect to the volume of the solid's reference configuration $\mathcal{B}_0$. It is a function of the crack phase field $d \in [0, 1]$, which interpolates between the unbroken and the broken state of the material in the sense of a scalar damage variable. The function γ_l can be motivated by a prescribed shape of the regularization of sharp cracks, as considered in Miehe et al. [1], but also appeared before in Γ-convergence regularizations of free discontinuity problems as proposed in Ambrosio and Tortorelli [6,7], Dal Maso [8] and Braides [9,10]. The crack surface density function γ_l provides the starting point for a continuum damage formulation of fracture. In particular, *surface integrals* defined on sharp crack surfaces $\Gamma \subset \mathcal{B}_0$ are *approximated by volume integrals*, such as the critical fracture energy

$$\int_\Gamma g_c\, dA \approx \int_{\mathcal{B}_0} g_c \gamma_l\, dV, \tag{2}$$

where g_c is Griffith's critical energy release. Hence, $g_c\gamma_l$ can be viewed as a critical *fracture energy* measured with respect to the unit volume of the solid's reference configuration. Assuming an elastic free energy storage function $\psi(\nabla\boldsymbol{\varphi}; d)$ in the bulk of the solid depending on the deformation gradient $\nabla\boldsymbol{\varphi}$, that degrades for increasing phase field d, the *evolution of the phase field* was proposed in Miehe et al. [1] as a non-smooth, local evolution equation

$$\dot{d} = \frac{1}{\eta}\Big\langle -\frac{\delta(\psi + g_c\gamma_l)}{\delta d}\Big\rangle. \tag{3}$$

This equation *modifies* classical Ginzburg–Landau- or Allen–Cahn-type evolution equations to a phase field model of fracture, where the phase field is interpreted as a local, monotonously growing damage variable. It makes the evolving phase field dependent on the variational derivative of a total energy density, consisting of the elastic bulk energy ψ and the regularized surface energy $g_c\gamma_l$. The parameter η plays the role of a viscosity for the crack evolution and provides for $\eta \to 0$ the *rate-independent limit*. The non-smooth structure of (3), governed by the Macaulay bracket $\langle\cdot\rangle$, as well as the interpretation of the parameter η as a viscous regularization that may vanish, marks a key difference to the smooth phase field models of fracture proposed by Hakim and Karma [11], Karma et al. [12], Eastgate et al. [13] and Kuhn and Müller [14], which are based on the classical Ginzburg–Landau equation. It is also different from the variational theory of brittle fracture proposed by Francfort and Marigo [15], Bourdin et al. [16], that uses the above mentioned concepts of Γ-convergence by introducing a scalar auxiliary field in a global variational context, without arriving at a local evolution equation of the type given in Eq. (3).

Note that Eqs. (1)–(3) contain the basic ingredients of brittle fracture mechanics, however, in a regularized continuum sense of *gradient damage mechanics*. The formulation can be embedded into the general theory of gradient-extended dissipative continua with length scales, such as outlined in a general context in Capriz [17], Mariano [18], Frémond [19] and the recent work Miehe [20] on its variational structure. In particular, our approach to phase field fracture is conceptually in line with theories of gradient damage outlined in Frémond and Nedjar [21] and Peerlings et al. [22], Comi [23], Comi and Perego [24], however, with *critical differences* in the choice of the free energy and dissipation potential functions. We refer to Pham et al. [25] for a recent account on the relationship between damage and brittle fracture mechanics. Recall that finite-element-based numerical implementations of *sharp* crack discontinuities, such as interface element formulations (Xu and Needleman [26], Ortiz and Pandolfi [27], Miehe and Gürses [28], Gürses and Miehe [29]), element enrichment strategies (Simo et al. [30], Oliver [31,32], Linder and Armero [33]) and nodal enrichment strategies (Moës et al. [34], Wells and Sluys [35], Gasser and Holzapfel [36], Belytschko et al. [37], Song and Belytschko [38]) suffer in three-dimensional applications with complex crack branching. In contrast, the phase-field-type *diffusive* crack approach is a spatially smooth continuum formulation that avoids the modeling of

discontinuities and can be implemented in a straightforward manner by coupled multi-field finite element solvers. In Miehe et al. [1,2], complex crack patterns were modeled without any changes of regular finite element discretizations for sufficiently fine mesh resolutions.

1.2. Geometric generalization towards multi-physics problems

In this work, we generalize our above mentioned treatment towards a *rigorous geometric approach* to phase field fracture in *multi-physics problems*. The overall goal is to design a continuum theory of crack propagation applicable in a *modular format* to a large spectrum of coupled multi-field problems. The formulation is specified to the model problem of thermo-elasticity at finite strains. The novel aspects are:

- a purely *geometric and modular approach* to the phase field modeling of fracture based on the introduction of a *balance equation for a regularized crack surface*,
- the construction of *alternative crack driving forces*, including energetic, maximum stress and maximum strain criteria, which account for fracture in tension and possibly anisotropic stress response,
- a *full thermodynamical set up* for phase field fracture, applied to the model problem of thermo-elasticity at finite strains, *including all thermo-mechanical coupling effects*,
- particular assumptions for the *degradation of non-mechanical fluxes* at cracks and the incorporation of *additional constitutive functions* for fluxes on generated crack faces.

The investigation starts in Section 2 with an outline of a purely geometric approach to the phase field modeling of fracture. This results in the definition of a constitutive balance equation for the diffusive crack surface

$$\frac{d}{dt}\Gamma_l(d) = \frac{1}{l}\int_{\mathcal{B}_0}[(1-d)\mathcal{H} - \mathcal{R}]\dot{d}\,dV \tag{4}$$

that governs the evolution of the crack phase field. The right-hand side includes two constitutive functions, the local *crack driving force* $\mathcal{H}$ and a *viscous crack resistance* $\mathcal{R}$. These functions provide the only impact from a multi-physics bulk response towards the crack evolution. Their introduction offers a strong flexibility with regard to the use of alternative fracture criteria. The restriction to *irreversible* crack propagation, i.e. local crack growth $\dot{d} \geq 0$ and positive crack driving force $\mathcal{H} \geq 0$, induce a representation of the crack driving force

$$\mathcal{H}(\boldsymbol{X}, t) = \max_{s\in[0,t]} \tilde{D}\big(state(\boldsymbol{X}, s)\big) \tag{5}$$

in terms of a *crack driving state function* $\tilde{D}$, depending on a set *state* of state variables of the multi-physics bulk response. This constitutive function provides the key impact from the bulk response to the crack evolution. The evolution equation (4) characterizes a purely geometric approach to the phase field modeling of fracture, that considers the regularized crack surface Γ_l as the central object. A *modular computational tool* is designed that updates the crack surface Γ_l based on a finite element discretization of the crack phase field. Such a tool offers a simple algorithm for crack updates, that can be linked for *any* crack driving state function $\tilde{D}$ to *any* multi-physics problem via *one-pass operator splits* or *Gauss–Seidel-type iterations* between crack and bulk response. This crack surface update tool is summarized in Boxes I and II.

We then generalize in Section 3 the energetic and variational-based approach of brittle fracture outlined in Miehe et al. [1,2] towards alternative crack driving criteria. This includes the definition of a crack driving state function

$$\tilde{D} = \Big\langle \sum_{a=1}^{3} (\langle\tilde{\sigma}_a\rangle/\sigma_c)^2 - 1 \Big\rangle \tag{6}$$

that realizes a *maximum principal stress criterion* with a critical fracture stress threshold σ_c. Such a definition makes the differentiation between tensile and compression regions simple and is open with regard to extensions towards complex anisotropies in the constitutive modeling. We outline elementary investigations on the performance of alternative driving forces, which favor the above stress-based approach. The proposed concept for the modeling of phase field fracture can be linked in a *modular format* to different types of multi-physics scenarios. This includes

the steps:

1. Modeling of the undamaged *nominal bulk response* of the multi-physics problem.
2. Construction of *transition rules* from unbroken to the fully broken bulk response, where the fracture phase field enters as a geometric internal variable.
3. Modeling the *crack driving state function* in the balance equation for the regularized crack surface, that governs the evolution of the fracture phase field.

This modular concept induces in a natural format the staggered algorithmic scheme in Box I, that decouples in a typical time step the update of the crack phase field from the update of the multi-physics bulk response.

As a model problem, we consider in Sections 4 and 5 a formulation of *finite thermo-elasticity coupled with fracture*. This covers a careful outline of the general equations in Section 4 and a simple constitutive model problem in Section 5. All equations are outlined in a rigorous Lagrangian geometric setting with respect to the reference configuration. It accounts for coupling to the phase field modeling of crack propagation outlined in Section 2 via the above mentioned steps 2 and 3. The evolution of the crack phase field is considered as a *purely dissipative effect* that produces heat. In this context, the evolution of the crack surface enters the phase field evolution as a *geometric resistance*. The modeling of the bulk response is essentially restricted to the modeling of the *nominal response* of the undamaged material and a particular assumption concerning the *transition rules* which model the degradation of selected parts such as the elastic stored energy. Here, the fracture phase field enters the key constitutive functions for the energy storage and dissipation potential functions as a *geometric effect*, governed by the evolution equation summarized in Box II.

The constitutive functions are specified for a model problem in Section 5. In this context, we outline a concept for the *constitutive definition of non-mechanical fluxes at the crack faces*. This is achieved by approximating surface integrals of the sharp crack approach by distinct volume integrals. As a consequence, a *conduction across a crack* is modeled by a degrading heat flux dissipation function for the solid-freespace mixture. A *convective heat exchange* is described by an extra contribution to the bulk heat source.

For this coupled bulk response, consisting of the mechanical deformation field and the temperature field, we comment in Section 6 on a monolithic solution scheme. Practical investigations use an operator splitting technique with an elastic predictor, followed by a heat conduction corrector, that is combined with a one-pass operator split or a Gauss–Seidel iteration in Box I with the update of the crack phase field. Such an algorithmic setting is extremely robust and considered to be the most simple scheme for the treatment of diffusive fracture in thermo-elastic solids. Finally, Section 8 outlines representative numerical examples which demonstrate fundamental geometric and physical coupling effects in thermo-elastic solids at fracture. These are the generation of heat due to cracking, inducing an increase of temperature, the degradation of non-mechanical bulk fluxes at crack surfaces, the appearance of new fluxes at the generated crack surfaces as well as the generation of cracks due to thermally induced stress states.

2. A purely geometric approach to phase field fracture

2.1. The definition of a regularized crack surface functional

The idea of regularizing a sharp crack topology by a diffusive crack topology based on the introduction of a crack phase field d was motivated in Miehe et al. [1]. Let $\mathcal{B}_0 \subset \mathcal{R}^\delta$ be the reference configuration of a material body with dimension $\delta \in [2, 3]$ in space and $\partial\mathcal{B}_0 \subset \mathcal{R}^{\delta-1}$ its surface as depicted in Fig. 1. We consider the crack phase field

$$d : \begin{cases} \mathcal{B}_0 \times \mathcal{T} \to [0, 1] \\ (\boldsymbol{X}, t) \mapsto d(\boldsymbol{X}, t) \end{cases} \tag{7}$$

characterizing for $d = 0$ the unbroken and for $d = 1$ the fully broken state of the material at $\boldsymbol{X} \in \mathcal{B}_0$. The parameter $t \in \mathcal{R}$ is for rate-dependent problems the time, for rate-independent problems an incremental loading parameter. In Miehe et al. [1], starting from an *assumed regularization profile* of a sharp crack at $x = 0$ by the exponential function $\exp[-|x|/l]$ as indicated in Fig. 3(b), a regularized crack surface functional was derived

$$\boxed{\Gamma_l(d) = \int_{\mathcal{B}_0} \gamma_l(d, \nabla d)\, dV} \tag{8}$$

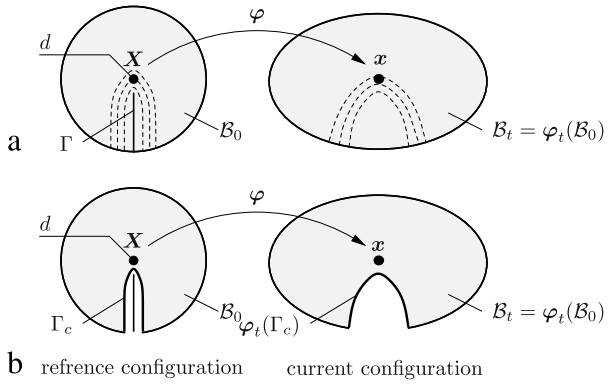

Fig. 1. Finite deformation of a body with a regularized crack. The *deformation map* $\boldsymbol{\varphi}$ maps at time $t \in \mathcal{T}$ the reference configuration $\mathcal{B}_0 \in \mathcal{R}^\delta$ onto the current configuration $\mathcal{B}_t$. (a) The *crack phase field* $d \in [0, 1)$ defines a regularized crack surface functional $\Gamma_l(d)$ that converges in the limit $l \to 0$ to the sharp crack surface Γ. (b) The level set $\Gamma_c = \{\boldsymbol{X} \mid d = c\}$ defines for a constant $c \approx 1$ the crack faces in the regularized setting. Parts of the continuum with $d > c$ are considered to be free space and are not displayed.

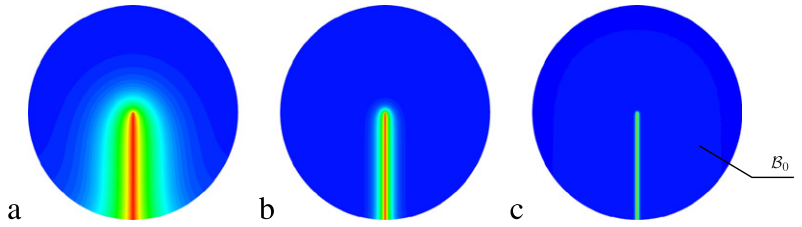

Fig. 2. Continuum approximation of crack discontinuities. Solutions of the variational problem (10) of diffusive crack topology for a circular specimen with a given sharp crack Γ, prescribed by the Dirichlet condition $d = 1$. Crack phase field $d \in [0, 1]$ for different length scales $l_a > l_b > l_c$. The sequence of plots visualizes the limit $\Gamma_l \to \Gamma$ of the regularized crack surface functional (8) towards the sharp crack surface.

in terms of an isotropic *crack surface density function* per unit volume of the solid

$$\gamma_l(d, \nabla d) = \frac{1}{2l} d^2 + \frac{l}{2} |\nabla d|^2 \tag{9}$$

that satisfies $\gamma_l(d, \nabla d) = \gamma_l(d, \boldsymbol{Q}\nabla d)$ for all $\boldsymbol{Q} \in SO(3)$. This function, which depends on the crack phase field d and its spatial gradient ∇d, plays the central role in the subsequent modeling of crack propagation. It coincides with terms obtained in Γ-convergent regularizations of free discontinuity problems outlined in Ambrosio and Tortorelli [6] and is governed by the length scale parameter l. Assuming a given sharp crack surface topology $\Gamma(t) \subset \mathcal{R}^{\delta-1}$ inside the solid $\mathcal{B}_0$ at time t, we obtain the regularized crack phase field $d(\boldsymbol{X}, t)$ on $\mathcal{B}_0$ from the *minimization principle of diffusive crack topology*

$$d(\boldsymbol{X}, t) = \arg\Big\{ \inf_{d \in W_{\Gamma(t)}} \Gamma_l(d) \Big\} \tag{10}$$

subject to the Dirichlet constraint $W_{\Gamma(t)} = \{d \mid d(\boldsymbol{X}, t) = 1 \text{ at } \boldsymbol{X} \in \Gamma(t)\}$. The Euler equations of this variational principle are

$$d - l^2 \Delta d = 0 \quad \text{in } \mathcal{B}_0 \quad \text{and} \quad \nabla d \cdot \boldsymbol{n}_0 = 0 \quad \text{on } \partial\mathcal{B}_0, \tag{11}$$

where Δd is the Laplacian of the phase field and $\boldsymbol{n}_0$ the outward normal on $\partial\mathcal{B}_0$.

The above mentioned exponential ansatz is a solution of (11) for the one-dimensional problem with Dirichlet condition $d = 1$ at $x = 0$. Fig. 2 depicts numerical solutions of the variational problem (10) for two-dimensional

problems, which demonstrate the influence of the length scale l. Note that the limit of the principle (10), i.e.

$$\lim_{l\to 0}\Big\{\inf_{d\in W_{\Gamma(t)}} \Gamma_l(d)\Big\} = \Gamma(t) \tag{12}$$

gives for vanishing length scale $l \to 0$ the *sharp crack surface* Γ. In the subsequent continuum setting of regularized crack discontinuities, the image of the functional $\Gamma_l(d)$ is considered to be the crack surface itself. A more detailed and intuitive derivation of the above formulation is outlined in Miehe et al. [1].

2.2. Constitutive balance equation for regularized crack surface

We develop a generalized formulation for the evolution of the phase field $d(\boldsymbol{X}, t)$ that is open for different constitutive models of energetic and non-energetic driving forces, i.e. suitable for the application to brittle and ductile fracture. Keeping in mind a purely geometric picture, we *postulate* the evolution of the crack surface functional defined in (8)

$$\boxed{\frac{d}{dt}\Gamma_l(d) = S(d, \dot{d}, \mathcal{H})} \tag{13}$$

to be driven by a *constitutive crack driving functional* S. This power is assumed to depend on the crack phase field d, its rate $\dot{d}$ and a *local crack driving force field* $\mathcal{H}$ that depends on the full history of the local bulk response under consideration, such as the energetic state or the stress state of the solid. The above equation can be viewed as a balance of crack surface, that equalizes the rate of crack generation with the power of crack driving force.

2.2.1. Geometric crack resistance

The evolution of the regularized crack surface can be recast into the form

$$\frac{d}{dt}\Gamma_l = \frac{1}{l}\int_{\mathcal{B}_0} D_c \dot{d}\, dV + \int_{\partial\mathcal{B}_0} (\partial_{\nabla d}\gamma \cdot \boldsymbol{n}_0)\dot{d}\, dA, \tag{14}$$

where $\boldsymbol{n}_0$ is the outward normal on $\partial\mathcal{B}_0$. The function D_c is a dimensionless *geometric crack resistance* associated with the regularization (8) of the sharp crack surface. It is related to the variational derivative of the crack density function γ_l introduced in (9) by

$$D_c := l\delta_d\gamma_l = d - l^2\Delta d. \tag{15}$$

2.2.2. Constitutive crack driving functional

In analogy to the first term in (14) we write the crack driving source in (13) as the power expression

$$\boxed{S = \frac{1}{l}\int_{\mathcal{B}_0} [(1-d)\mathcal{H} - \mathcal{R}]\dot{d}\, dV} \tag{16}$$

Here, $\mathcal{H}$ is the *local crack driving force* and $\mathcal{R}$ a *local viscous crack resistance*. Both fields are assumed to be governed by constitutive expressions. We assume the simple dependence

$$\mathcal{R}(\boldsymbol{X}, t) = \tilde{\mathcal{R}}(\dot{d}(\boldsymbol{X}, t)) \quad \text{and} \quad \mathcal{H}(\boldsymbol{X}, t) = \tilde{\mathcal{H}}((state(\boldsymbol{X}, s), 0 \le s \le t)). \tag{17}$$

Hence, the viscous crack resistance $\mathcal{R}$ is assumed to be in a one-to-one relationship to the rate $\dot{d}(\boldsymbol{X}, t)$ of the phase field. The driving force $\mathcal{H}$ depends on the full history at $0 \le s \le t$ of state variables $state(\boldsymbol{X}, s)$ associated with the solid's bulk response. This may cover the history of the *energetic state*, the *stress state* or selected *internal variables*. In what follows, we focus on the simple constitutive function

$$\tilde{\mathcal{R}} = \eta\dot{d} \tag{18}$$

for the viscous crack resistance, where $\eta \ge 0$ is a material parameter that characterizes the viscosity of the crack propagation. $\eta = 0$ models rate-independent propagation.

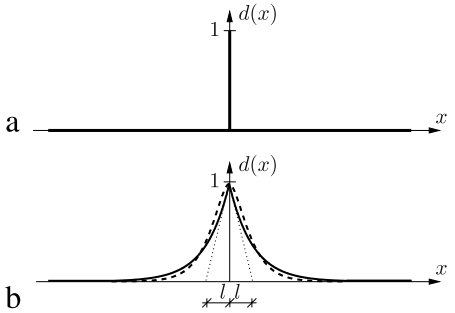

Fig. 3. Sharp and diffusive crack modeling. (a) Sharp crack at $x = 0$. (b) Diffusive crack at $x = 0$ modeled with the length scale l. Regularized curves obtained from minimization principle of diffusive crack topology $\int_{\mathcal{B}_0} \gamma_l \, dV \rightarrow Min!$ with crack surface density function γ_l. Thick line: $\gamma_l = d^2/2l + l|\nabla d|^2/2$ with regularization profile $\exp[-|x|/l]$ satisfying $d(0) = 1$, dotted line: $\gamma_l = d^2/2l + l|\nabla d|^2/4 + l^3(\Delta d)^2/32$ with regularization profile $\exp[-2|x|/l](1 + 2|x|/l)$ satisfying $d(0) = 1$ and $d'(0) = 0$.

2.2.3. Evolution equation for crack phase field

The global evolution statement (13) for the crack surface induces for rates $\dot{d} \neq 0$ a local equation for the evolution of the crack phase field

$$\underbrace{\eta \dot{d}}_{\text{evolution}} = \underbrace{(1-d)\tilde{\mathcal{H}}}_{\text{driving force}} - \underbrace{[d - l^2 \Delta d]}_{\text{geometric resistance}} \tag{19}$$

in the domain $\mathcal{B}_0$, along with a homogeneous Neumann condition

$$\nabla d \cdot \boldsymbol{n}_0 = 0 \quad \text{on } \partial\mathcal{B}_0. \tag{20}$$

Eq. (19) makes the evolution of the crack phase field dependent on the difference $(1-d)\tilde{\mathcal{H}} - D_c$ between the effective driving force $(1-d)\tilde{\mathcal{H}}$ and the geometric crack resistance D_c. It is viewed as a *generalized Ginzburg–Landau-type structure*, when the right hand side follows from the variational derivative of a *total energy expression* as considered in Eq. (3) of the introduction. Note carefully, that the above framework covers the *rate-independent limit* for $\eta = 0$, where the crack surface is simply defined by an equilibrium between crack driving force and geometric crack resistance.[1]

2.3. Constraints on driving force for irreversible crack evolution

Within this work, we focus on an irreversibility of the crack evolution, governed by the constraint

$$\frac{d}{dt}\Gamma_l(d) = S \geq 0 \tag{23}$$

[1] *Higher Order Approach to Regularization of Crack Topology*. A fourth-order approach to a regularized crack topology was recently proposed by Borden et al. [4] based on the extension of the crack surface density function (9) by a term depending on the Laplacian of the phase field

$$\gamma_l(d, \nabla d, \Delta d) = \frac{1}{2l}d^2 + \frac{l}{4}|\nabla d|^2 + \frac{l^3}{32}(\Delta d)^2. \tag{21}$$

It approximates a sharp crack discontinuity by a profile $\exp[-2|x|/l](1+2|x|/l)$ with higher regularity, as indicated by the dotted line in Fig. 3(b). Insertion into the evolution equation for the crack surface (13) gives a fourth-order extension of (19)

$$\eta\dot{d} = (1-d)\mathcal{H} - \Big[d - \frac{l^2}{2}\Delta d + \frac{l^4}{16}\Delta(\Delta d)\Big] \tag{22}$$

with an additional fourth-order term in the geometric crack resistance. The associated boundary conditions are $\nabla[d - (l^2/8)\Delta d] \cdot \boldsymbol{n}_0 = 0$ and $\Delta d = 0$ on $\partial\mathcal{B}_0$. This shows the generality of the proposed geometric approach based on the balance-type equation (13), that is open for alternative choices of the crack surface density function. However, as shown in Borden et al. [4], the higher-order approximation (21) comes with additional cost with respect to the numerical implementation. In this work, we restrict the subsequent formulation to the density function (9).

on the evolution of the regularized crack surface. Hence, the *constitutive crack driving power* (13) must be positive. Taking into account the assumed representation (16), this is achieved for the physically-based restrictions

$$\begin{aligned} &1.\ \text{bounded phase field } d \in [0,1], \\ &2.\ \text{local crack growth } \dot{d} \geq 0, \\ &3.\ \text{positive driving force } \mathcal{H} \geq 0. \end{aligned} \tag{24}$$

These conditions ensure a growth of the crack surface up to the fully broken state. The condition equation $(24)_1$ demands locally that the phase field d, which starts from the initial condition $d = 0$ for the unbroken state, is bounded by $d < 1$ when cracks accumulate. In order to get further insight to the constitutive definition of the driving force $\mathcal{H}$, consider a *rate-independent* crack growth with $\eta = 0$ for a *homogeneous problem* with $\nabla d = 0$. Then (19) gives a one-to-one relationship between the crack phase field d and the nominal driving force $\mathcal{H}$. As a consequence, conditions $(24)_{1,2}$ can be recast into the constraints

$$d = \frac{\mathcal{H}}{1+\mathcal{H}} \in [0,1] \quad \text{and} \quad \dot{d} = \frac{\dot{\mathcal{H}}}{(1+\mathcal{H})^2} \geq 0 \tag{25}$$

on the driving force $\mathcal{H}$ and its evolution $\dot{\mathcal{H}}$, which must be satisfied by the constitutive expression $(17)_2$. Clearly, as indicated by $(25)_1$, locally unbroken and fully broken states are associated by

$$d = 0 \Leftrightarrow \mathcal{H} = 0 \quad \text{and} \quad d = 1 \Leftrightarrow \mathcal{H} \to \infty. \tag{26}$$

Taking into account these relationships, the constitutive function $\tilde{\mathcal{H}}$ in $(17)_2$ for the crack driving force in $(17)_2$ must satisfy the following three constraints

$$\boxed{\tilde{\mathcal{H}}\big|_{\text{state}}^{\text{unbroken}} = 0\,, \quad \tilde{\mathcal{H}}\big|_{\text{state}}^{\text{broken}} = \infty\,, \quad \frac{d}{dt}\tilde{\mathcal{H}} \geq 0} \tag{27}$$

for the unbroken initial state, the fully broken state and its evolution in time. Hence, the constitutive driving force $\tilde{\mathcal{H}}$ must be a *positive, monotonously growing function*. Note, that in the case of a *non-homogeneous response* the determining Eq. (19) for the phase field

$$\Delta d - \frac{1+\mathcal{H}}{\ell^2} d = -\frac{\mathcal{H}}{\ell^2} \quad \text{in } \mathcal{B}_0 \tag{28}$$

together with its Neumann boundary condition (20) also leads to a solution bounded by $d \in [0,1]$ for $\mathcal{H} \geq 0$. This follows from the *maximum principle of elliptic partial differential equations*, see Protter and Weinberger [39].

2.4. Non-smooth evolution of cracks with loading and unloading

Consider an arbitrary evolution of the state variables $state(\boldsymbol{X}, t)$ associated with the bulk response in time, related to a loading and an unloading of the solid under consideration. Then, the growth condition $(27)_3$ on the constitutive crack driving force is satisfied by the ansatz

$$\boxed{\tilde{\mathcal{H}}(\boldsymbol{X}, t) = \max_{s \in [0,t]} \tilde{D}(state(\boldsymbol{X}, s))} \tag{29}$$

that partially specifies the constitutive function $(17)_2$. This assumes the driving force $\tilde{\mathcal{H}}$ at a position $\boldsymbol{X} \in \mathcal{B}_0$ and current time $t \in \mathcal{T}$ as the *maximum value* of an associated *crack driving state function* $\tilde{D}$ obtained in the full process history $s \in [0,t] \subset \mathcal{T}$. The remaining conditions $(27)_{1,2}$ are then satisfied for the constraint

$$\tilde{D}\big|_{\text{state}}^{\text{unbroken}} = 0 \quad \text{and} \quad \tilde{D}\big|_{\text{state}}^{\text{broken}} = \infty \tag{30}$$

on the crack state function $\tilde{D}$. Within the framework proposed here based on the evolution equation for a regularized crack surface, this function provides the *key link to the solid's bulk response*. Particular forms for brittle fracture are

1. *Initialize Crack Driving Force*. Explicit definition of the crack driving force
$$\mathcal{H} = \mathcal{H}_n$$
2. *Update of Crack Surface*. Compute current crack phase field by the *linear* algorithm summarized in Box II
$$\boxed{d = ALGO_2(\mathcal{H})}$$
3. *Update of Bulk Response*. For given crack phase field d, update the *non-linear* bulk response by an iterative procedure summarized in Section 6, using a *crack transition rule* for the constitutive functions $\hat{\boldsymbol{f}}$, e.g. of the form
$$\hat{\boldsymbol{f}}(state; d) = g^s(d)\tilde{\boldsymbol{f}}^s(state) + g^c(d)\tilde{\boldsymbol{f}}^c(state)$$
4. *Update Crack Driving Force*. For given state variables $state(\boldsymbol{X}, s)$ of bulk response, update crack driving force based on constitutive crack driving state function $\tilde{D}$
$$\mathcal{H}(\boldsymbol{X}, t) = \max_{s\in[0,t]} \tilde{D}(state(\boldsymbol{X}, s))$$
5. *Multi-Pass Solution*. For a Jacobi-type multi-pass solution of the crack surface and bulk response, go to 2 until convergence is achieved.

Box I. $ALGO_1$: Updates of Crack Surface and Bulk Response in $[t_n, t]$.

discussed in the subsequent Section 3. Note that the ansatz (29) in combination with the evolution equation (19) for the phase field is consistent with the structure

$$\eta\dot{d} = \left\langle (1-d)\tilde{D} - l\delta_d\gamma_l \right\rangle \geq 0, \tag{31}$$

where $\langle x\rangle := (x + |x|)/2$ is the Macaulay bracket. Hence, a non-smooth evolution of the crack phase field takes place when the effective state function $(1-d)\tilde{D}$ exceeds the geometric crack resistance $l\delta_d\gamma_l$. For the rate-independent limit $\eta \to 0$, the associated local evolution system is

$$\dot{d} \geq 0, \qquad [(1-d)\tilde{D} - l\delta_d\gamma_l] \leq 0, \qquad \dot{d}[(1-d)\tilde{D} - l\delta_d\gamma_l] = 0. \tag{32}$$

Observe again that the dimensionless crack state function $\tilde{D}$ is the key constitutive input on the driving side, while the dimensionless geometric crack resistance $D_c := l\delta_d\gamma_l$ is related to the variational derivative of the crack surface density function γ_l.

2.5. Incremental update of regularized crack surface and operator split

The integration of (13) in the time interval $[t_n, t_{n+1}]$ gives an update for the regularized crack surface. In what follows, all variables without a subscript are time discrete values at the current solution time t_{n+1}. A robust algorithm for the update of the phase field is obtained by an operator splitting, keeping the driving force constant in the time step

$$\mathcal{H} = \text{constant in } [t_n, t_{n+1}]. \tag{33}$$

Note that this driving force provides the impact from the bulk response to the crack evolution. The above assumption covers for the *one-path* algorithm $ALGO_1$ in Box I a *semi-implicit* time integration of the phase field. For the *multi-path* algorithm $ALGO_1$, where $\mathcal{H}$ is corrected, an implicit update scheme with *Gauss–Seidel-type iterations* between the phase field $d(\boldsymbol{X}, t)$ and the state variables $state(\boldsymbol{X}, t)$ of the bulk response is obtained. In both cases, (33) induces an algorithmic decoupling of updates for the phase field and the bulk response in the time interval under consideration and is the key ingredient of a *modular implementation of phase field fracture*. The algorithms $ALGO_1$ and $ALGO_2$ in Boxes I and II provide a *crack update module* applicable to a wide spectrum of problems. The one-path algorithm for $\mathcal{H} = \mathcal{H}_n$ is in line with the treatment of Miehe et al. [2].

Time integration of (13) gives for $\mathcal{H} =$ const. the closed form update for the crack surface

$$\Gamma_l(d) = \Gamma_l(d_n) + \frac{1}{l}\int_{\mathcal{B}_0} \left\{ \left[(d - d_n) - \frac{1}{2}(d^2 - d_n^2) \right]\mathcal{H} - \frac{\eta}{2\tau}(d - d_n)^2 \right\} dV. \tag{34}$$

1. *Evolution of Crack Surface*. The postulate of a global evolution equation for the regularized crack surface

$$\frac{d}{dt}\Gamma_l(d) = \frac{1}{l}\int_{\mathcal{B}_0}[(1-d)\mathcal{H} - \eta\dot{d}]\dot{d}\,dV$$

with the crack surface density function $\gamma_l = d^2/2l + l|\nabla d|^2/2$ results for boundary condition $\nabla d \cdot \boldsymbol{n}_0 = 0$ on $\partial\mathcal{B}_0$ in the evolution equation for the phase field $d \in [0, 1)$

$$\boxed{\eta\dot{d} = (1-d)\mathcal{H} - [d - l^2\Delta d]}$$

2. *Incremental Update of Crack Surface*. Semi-implicit time integration in $[t_n, t]$ with crack driving force $\mathcal{H} = const.$ gives update of crack surface

$$\Gamma_l(d) = \Gamma_l(d_n) + \frac{1}{l}\int_{\mathcal{B}_0}\Big\{\Big[(d-d_n) - \frac{1}{2}(d^2 - d_n^2)\Big]\mathcal{H} - \frac{\eta}{2\tau}(d-d_n)^2\Big\}\,dV$$

and induces the linear equation for the update of the crack phase field

$$\boxed{\eta(d-d_n)/\tau = (1-d)\mathcal{H} - [d - l^2\Delta d]}$$

3. *Finite Element Update of Crack Surface*. Space discretization of phase field state $\mathfrak{c}_d^h := \{d^h, \nabla d^h\} = \boldsymbol{B}_d\boldsymbol{d}_d$ and optimization of the incremental potential

$$\Pi_d^{\tau\,h}(\boldsymbol{d}_d) = \int_{\mathcal{B}_0^h}\pi_d^\tau(\boldsymbol{B}_d\boldsymbol{d}_d)\,dV$$

with the potential density function

$$\pi_d^\tau = \frac{\eta}{2\tau}(d-d_n)^2 + l\gamma_l(d,\nabla d) - l\gamma_l(d_n,\nabla d_n) - \Big[(d-d_n) - \frac{1}{2}(d^2-d_n^2)\Big]\mathcal{H}$$

results in linear update of nodal degrees of the phase field in $[t_n, t]$

$$\boxed{\boldsymbol{d}_d = -[\Pi_d^{\tau\,h}]^{-1}_{,\boldsymbol{d}_d\boldsymbol{d}_d}[\Pi_d^{\tau\,h}]_{,\boldsymbol{d}_d}}$$

Box II. $ALGO_2$: Evolution and Update of Crack Surface for Given Force $\mathcal{H}$.

Multiplying by the length scale l and arranging all terms on the left hand side define a *quadratic potential*

$$\Pi_d^\tau(d) = \int_{\mathcal{B}_0}\pi_d^\tau(\mathfrak{c}_d)\,dV = 0 \tag{35}$$

in terms of the quadratic potential density per unit of the reference volume

$$\pi_d^\tau(\mathfrak{c}_d) = \frac{\eta}{2\tau}(d-d_n)^2 + l\gamma_l(d,\nabla d) - l\gamma_l(d_n,\nabla d_n) - [(d-d_n) - \frac{1}{2}(d^2-d_n^2)]\mathcal{H} \tag{36}$$

that depends on the current phase field and its gradient $\mathfrak{c}_d := \{d, \nabla d\}$. As stated in (35), the potential $\Pi_d^\tau(d)$ must be stationary, attaining the minimum value zero for the current phase field d. Hence, the phase field is determined by the *minimization principle*

$$d = \arg\Big\{\inf_d \Pi_d^\tau(d)\Big\}. \tag{37}$$

The Euler equation of this minimization principle is the linear update equation for the crack phase field

$$\underbrace{\eta(d-d_n)/\tau}_{\text{crack update}} = \underbrace{(1-d)\mathcal{H}}_{\text{driving force}} - \underbrace{[d - l^2\Delta d]}_{\text{geometric resistance}} \tag{38}$$

in the domain $\mathcal{B}_0$, along with the Neumann condition $\nabla d \cdot \boldsymbol{n}_0 = 0$ on $\partial\mathcal{B}_0$. Note that this provides in the one-path setting of algorithm $ALGO_1$ with $\mathcal{H} = \mathcal{H}_n$ a semi-implicit integration of the continuous equation (19). The link to the

bulk response is exclusively governed by the driving force $\mathcal{H}$. Keeping it constant, fully decouples the update of the crack phase field from the update of the constitutive response of the bulk. The update of the phase field is summarized in Box II. It can be performed *once* at the beginning of a typical time step, or eventually be embedded into a Gauss–Seidel-type *iteration* with the bulk response as outlined in Box I.

2.6. Finite element discretization of crack phase field update

The finite element implementation of the potential Π_d^τ in (35) is straightforward, yielding the space-discrete formulation

$$\Pi_d^{\tau\,h}(\boldsymbol{d}_d) = \int_{\mathcal{B}_0^h} \pi_d^\tau(\boldsymbol{B}_d \boldsymbol{d}_d)\, dV = 0 \tag{39}$$

based on the discretization $\mathfrak{c}_d^h(\boldsymbol{X}, t) = \boldsymbol{B}_d(\boldsymbol{X})\boldsymbol{d}_d(t)$ in terms of the finite element interpolation matrix $\boldsymbol{B}_d$ and the nodal values $\boldsymbol{d}_d$ of the phase field in a typical finite element mesh. The nodal values follow from the optimization problem

$$\boldsymbol{d}_d = \arg\big\{\inf_{\boldsymbol{d}_d} \Pi_d^{\tau\,h}(\boldsymbol{d}_d)\big\}, \tag{40}$$

for the quadratic space-discrete potential, yielding the closed-form update of the nodal values for the phase field

$$\boldsymbol{d}_d = -\Big(\int_{\mathcal{B}^h} \boldsymbol{B}_d^T[\partial^2_{\mathfrak{c}_d\mathfrak{c}_d}\pi_d^\tau(\boldsymbol{B}_d\boldsymbol{d}_{d\,n})]\boldsymbol{B}_d\, dV\Big)^{-1} \int_{\mathcal{B}^h} \boldsymbol{B}_d^T[\partial_{\mathfrak{c}_d}\pi_d^\tau(\boldsymbol{B}_d\boldsymbol{d}_{d\,n})]\, dV. \tag{41}$$

Note again that this solution is independent from the finite element updates of the bulk response due to the algorithmic decoupling within the time step under consideration. The only impact from the bulk response is provided by the driving force $\mathcal{H}$ that enters the potential π_d^τ in (36), see Box II. Hence, this algorithm provides a *crack update tool* that can essentially be linked to any bulk response.

3. Driving forces for brittle failure and transition rules

As outlined in Box I, the impact from the bulk response on the crack propagation is governed by the crack driving force $\mathcal{H}$ that is linked to a constitutive *crack driving state function* $\tilde{D}(state)$. Vice versa, the crack phase field enters the bulk response via constitutive *transition rules* $\hat{\boldsymbol{f}}(state; d)$ from the unbroken to the broken state functions of the bulk material. This section outlines alternative structures of these functions, which are specified for a model problem in Section 4.

3.1. Crack driving state functions for different failure criteria

The only point that remains to make the phase field equation (31) and (32) concrete is the definition of the crack state function $\tilde{D}$. This makes the formulation very flexible with regard to the incorporation of alternative crack driving criteria. In what follows, we outline some examples for brittle failure.

3.1.1. Evolution equations in gradient damage mechanics

A class of gradient damage approaches for the modeling of brittle fracture assumes a "*total*" *pseudo-energy density* W per unit volume, which contains the sum

$$W(\boldsymbol{\varepsilon}, d, \nabla d) = W_{bulk}(\boldsymbol{\varepsilon}; d) + W_{frac}(d, \nabla d) \tag{42}$$

of a *degrading elastic bulk energy* W_{bulk} and a *contribution due to fracture* W_{frac} that contains the accumulated dissipative energy. The bulk contribution is assumed to have the simple form

$$W_{bulk}(\boldsymbol{\varepsilon}; d) = (1-d)^2\tilde{\psi}(\boldsymbol{\varepsilon}), \tag{43}$$

where $\tilde{\psi}(\boldsymbol{\varepsilon})$ is the *effective energy* stored in the undamaged material and $g^s(d) = (1-d)^2$ a degradation function that satisfies the properties $W_{bulk}(\boldsymbol{\varepsilon}; 0) = \tilde{\psi}(\boldsymbol{\varepsilon})$, $W_{bulk}(\boldsymbol{\varepsilon}; 1) = 0$, $\partial_d W_{bulk}(\boldsymbol{\varepsilon}; d) < 0$ and $\partial_d W_{bulk}(\boldsymbol{\varepsilon}; 1) = 0$. In the finite deformation context, $\boldsymbol{\varepsilon}$ is Almansi's tensor as defined in Section 4. The above introduction of competing bulk and

surface energy densities is in line with treatment of gradient damage theories outlined in Frémond and Nedjar [21], Frémond [19] and the works of Benallal and Marigo [40] and Pham et al. [25], see also Miehe [20] for an embedding into variational principles. The evolution of the damage variable d is then determined by the *variational derivative* of W. In a rate-independent setting, this is provided by the Kuhn–Tucker-type equations

$$\dot{d} \geq 0, \qquad -\delta_d W \leq 0, \qquad \dot{d}[-\delta_d W] = 0. \tag{44}$$

These equations are shown in Miehe [20] to be the Euler equations of a rate-type variational principle for the evolution problem of gradient damage mechanics. They provide the basis for the *phase field modeling of brittle fracture* proposed by Miehe et al. [1].

3.1.2. Strain criterion without threshold

An energetic criterion without threshold used by Miehe et al. [1] is based on the fracture contribution to the "total" pseudo-energy (42)

$$W_{frac}(d, \nabla d) = g_c \gamma_l(d, \nabla d) = \frac{g_c}{2l}[d^2 + l^2 |\nabla d|^2]. \tag{45}$$

It is directly related to the crack surface density function γ_l defined in (8). Here, g_c is Griffith's critical energy release rate. Hence, a fracture surface energy per unit volume is obtained by multiplying Griffith's critical energy release rate g_c with the crack surface density function. The "total" pseudo-energy potential takes the form

$$W(\boldsymbol{\varepsilon}, d, \nabla d) = (1-d)^2 \tilde{\psi}(\boldsymbol{\varepsilon}) + g_c \gamma_l(d, \nabla d) \tag{46}$$

in terms of the two functions $\tilde{\psi}$ and γ_l. Then, the loading criterion (44) for the phase field includes the loading function

$$-\delta_d W = 2(1-d)\tilde{\psi}(\boldsymbol{\varepsilon}) - g_c \delta_d \gamma_l(d, \nabla d), \tag{47}$$

and can be recast into the form

$$\frac{g_c}{l}[d - l^2 \Delta d] = 2(1-d) \max_{s \in [0,t]} \tilde{\psi}(\boldsymbol{\varepsilon}(\boldsymbol{X}, s)), \tag{48}$$

see Miehe et al. [1]. The comparison with (19) and (29) identifies the *crack driving state function*

$$\boxed{\tilde{D} = \frac{2\tilde{\psi}(\boldsymbol{\varepsilon})}{g_c / l}} \tag{49}$$

Note that this driving force depends on the ratio of the locally stored effective elastic energy $\tilde{\psi}$ referred to the critical energy release rate g_c, that can be considered to be *smeared out over the length scale* l. The function $\tilde{\psi}(\boldsymbol{\varepsilon})$ is monotonously growing, and may be considered to be a norm of the strain $\boldsymbol{\varepsilon}$. Hence, the driving force is related to the amount of local distortion. Note that this criterion does not differentiate between tension and compression modes. A formulation based on decomposition of the free energy into tensile and compression parts was considered in Miehe et al. [1].

3.1.3. Strain criterion with threshold

The criterion (49) is a monotonously increasing function of the strains $\boldsymbol{\varepsilon}$, as shown in Figs. 4(a) and 5(a). As a consequence, a damage-type degradation already occurs at low stress levels. In order to avoid this effect, an energetic *criterion with threshold* can be constructed based on the fracture contribution to the "total" pseudo-energy (42), i.e.

$$W_{frac}(d, \nabla d) = 2\psi_c \left[d + \frac{l^2}{2} |\nabla d|^2 \right]. \tag{50}$$

Here, ψ_c is a *specific fracture energy per unit volume*. Note that, in contrast to the definition (45), the phase field d enters the formulation by a linear term. Such formulations of gradient damage mechanics are discussed in Frémond

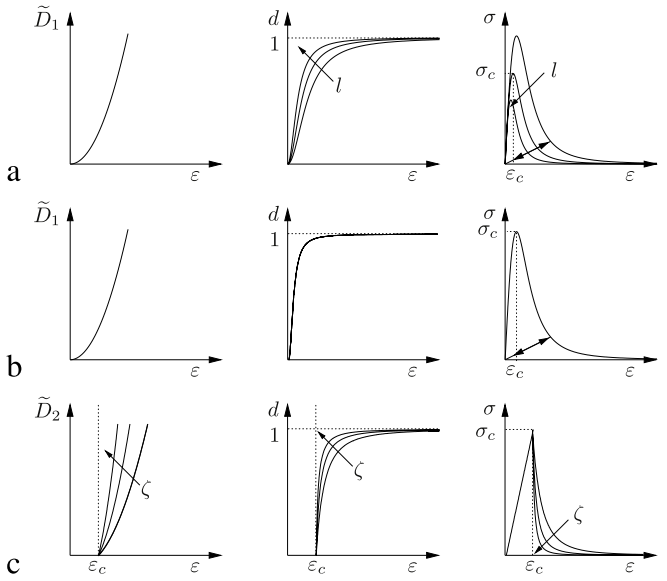

Fig. 4. Qualitative features of different driving forces in homogeneous test. Performance of (a) *energetic criterion* (49) with $\tilde{D}_1 = E\varepsilon^2/(g_c/l)$ for different length scale parameters l, (b) *energetic criterion* (49) for length-scale-dependent $g_c = 256\sigma_c^2 l/27E$ according to (68), (c) *maximum stress criterion* (61) with $\tilde{D}_2 = \zeta\langle(\tilde{\sigma}/\tilde{\sigma_c})^2 - 1\rangle$, where σ_c is the threshold of an elastic range.

and Nedjar [21], Frémond [19] and the recent contributions Pham et al. [25] and Miehe [20]. After some simple algebraic manipulation, the "total" energy potential (42) reads

$$W(\boldsymbol{\varepsilon}, d, \nabla d) = (1-d)^2[\tilde{\psi}(\boldsymbol{\varepsilon}) - \psi_c] + \psi_c + 2\psi_c l\gamma_l(d, \nabla d) \tag{51}$$

in terms of the crack surface density function γ_l defined in (8). Then, the loading criterion (44) for the phase field includes the loading function

$$-\delta_d W = 2(1-d)[\tilde{\psi}(\boldsymbol{\varepsilon}) - \psi_c] - 2\psi_c l\delta_d\gamma_l(d, \nabla d), \tag{52}$$

and can be recast into the form

$$2\psi_c[d - l^2\Delta d\,] = 2(1-d)\max_{s\in[0,t]}\left\langle\tilde{\psi}(\boldsymbol{\varepsilon}(\boldsymbol{X}, s)) - \psi_c\right\rangle. \tag{53}$$

The comparison with (19) and (29) identifies the *crack driving state function*

$$\boxed{\tilde{D} = \left\langle\frac{\tilde{\psi}(\boldsymbol{\varepsilon})}{\psi_c} - 1\right\rangle} \tag{54}$$

in terms of the ramp function $\langle x\rangle := (x + |x|)/2$ determined by the Macaulay bracket. Note that this criterion is independent of the length scale l, because the material parameter ψ_c for the specific fracture energy refers to the unit volume.

3.1.4. Stress criteria with and without threshold

In order to obtain a simple approach to brittle fracture that takes into account a decomposition into tension and compression, we develop a stress criterion. To this end, consider the Legendre–Fenchel transformation of the effective energy $\tilde{\psi}$ to its dual $\tilde{\psi}^*$

$$\tilde{\psi}^*(\tilde{\boldsymbol{\sigma}}) = \sup_{\boldsymbol{\varepsilon}}[\tilde{\boldsymbol{\sigma}} : \boldsymbol{\varepsilon} - \tilde{\psi}(\boldsymbol{\varepsilon})] \tag{55}$$

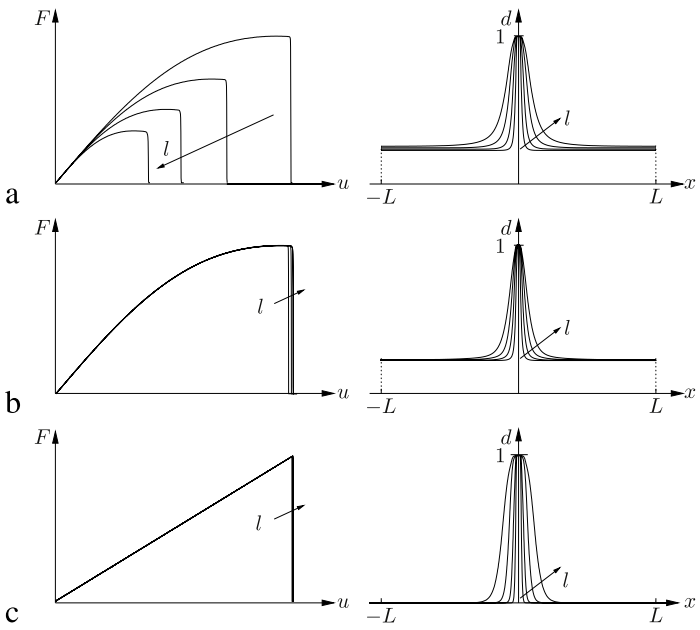

Fig. 5. Qualitative features of different driving forces in 1d finite element simulation. Performance of (a) *energetic criterion* (49) with $\tilde{D}_1 = E\varepsilon^2/(g_c/l)$, (b) *energetic criterion* (49) for length-scale-dependent $g_c = 256\sigma_c^2 l/27E$ according to (68), (c) *maximum stress criterion* (61) with $\tilde{D}_2 = \zeta\langle(\tilde{\sigma}/\sigma_c)^2 - 1\rangle$ for different length scale parameters l with $l/L = 0.004, 0.008, 0.016, 0.032$. Note that the threshold-type criterion (61) produces a limited band of the phase field profile and a remaining elastic range. Hence, this solution *converges* for $l \to 0$ to a sharp crack discontinuity.

in terms of the *effective Cauchy stresses* $\tilde{\boldsymbol{\sigma}} := \boldsymbol{\sigma}/(1-d)^2$. Insertion into (49) and (54) gives the alternative representations

$$\tilde{D} = \frac{2}{g_c/l}\big[\tilde{\boldsymbol{\sigma}} : \boldsymbol{\varepsilon} - \tilde{\psi}^*(\tilde{\boldsymbol{\sigma}})\big] \quad \text{and} \quad \tilde{D} = \Big\langle \frac{1}{\psi_c}[\tilde{\boldsymbol{\sigma}} : \boldsymbol{\varepsilon} - \tilde{\psi}^*(\tilde{\boldsymbol{\sigma}})] - 1 \Big\rangle \tag{56}$$

of the fracture driving forces in terms of the stress function $\tilde{\psi}^*$. Inspired by the *linear theory of elasticity* based on quadratic functions with identical images $\tilde{\psi}^*(\tilde{\boldsymbol{\sigma}}) = \tilde{\psi}(\boldsymbol{\varepsilon}) = \frac{1}{2}\tilde{\boldsymbol{\sigma}} : \boldsymbol{\varepsilon}$, we *postulate* the pure stress criteria

$$\tilde{D} = \frac{2\tilde{\psi}^*(\tilde{\boldsymbol{\sigma}})}{g_c/l} \quad \text{and} \quad \tilde{D} = \Big\langle \frac{\tilde{\psi}^*(\tilde{\boldsymbol{\sigma}})}{\psi_c} - 1 \Big\rangle \tag{57}$$

dual to (49) and (54), and apply it to nonlinear elasticity.

3.1.5. A principal tensile stress criterion with threshold

In order to obtain a simple criterion for mixed tensile-compression stress modes applicable to *general nonlinear and possibly anisotropic elasticity*, consider first the decomposition of the effective stress into tensile and compressive parts

$$\tilde{\boldsymbol{\sigma}} = \tilde{\boldsymbol{\sigma}}^+ + \tilde{\boldsymbol{\sigma}}^- \quad \text{with } \tilde{\boldsymbol{\sigma}}^+ := \sum_{a=1}^{3} \langle\tilde{\sigma}_a\rangle \boldsymbol{n}_a \otimes \boldsymbol{n}_a. \tag{58}$$

In a second step, define for the definition of the fracture driving force a quadratic effective stress function

$$\tilde{\psi}^*_{frac}(\tilde{\boldsymbol{\sigma}}^+) = \frac{1}{2E}\|\tilde{\boldsymbol{\sigma}}^+\|^2 = \frac{1}{2E}\sum_{a=1}^{3}\langle\tilde{\sigma}_a\rangle^2, \tag{59}$$

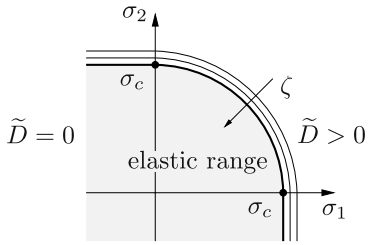

Fig. 6. Failure surface for tensile principle stress criterion (61). Stress states above the failure surface, determined by the critical fracture stress σ_c, raise the driving force function $\tilde{D}$ in (61), whose slope can be pronounced by the additional parameter $\zeta \geq 1$.

independent from the bulk response, where E is a parameter related to Young's modulus. Next, assume the critical fracture energy ψ_c per unit volume to be related to a *critical fracture stress* σ_c via

$$\psi_c := \frac{\sigma_c^2}{2E}. \tag{60}$$

Then, insertion of (59) and (60) into $(57)_2$ gives the simple isotropic *principal tensile stress* crack driving state function

$$\boxed{\tilde{D} = \zeta\Big\langle \sum_{a=1}^{3} \Big(\frac{\langle\tilde{\sigma}_a\rangle}{\sigma_c}\Big)^2 - 1\Big\rangle} \tag{61}$$

where an additional dimensionless parameter $\zeta > 0$ was introduced that influences for $\zeta \neq 1$ the growth of the crack phase field in the postcritical range. The crack state function provides a quadratically increasing barrier function for stress levels above a *failure surface in the principal stress space* determined by the critical tensile stress σ_c as depicted in Fig. 6, whose slope can be influenced by the parameter ζ. Such a criterion is extremely simple to implement, and applicable to brittle fracture in nonlinear, possibly anisotropic finite elasticity. It generalizes the classical maximum principle stress criterion, which can be traced back to Rankine, Lamé and Navier, to the phase field modeling of fracture. A pure Rankine-type criterion would be related to the phase field driving force

$$\tilde{D} = \zeta\Big\langle \frac{1}{\sigma_c^2} \max\big(\langle\tilde{\sigma}_1\rangle^2, \langle\tilde{\sigma}_2\rangle^2, \langle\tilde{\sigma}_3\rangle^2\big) - 1\Big\rangle. \tag{62}$$

It is related to the simple scenario of decohesion of surfaces perpendicular to the maximum principle stress. Figs. 4(c) and 5(c) demonstrate qualitative features of the criterion (61). In particular, Fig. 5(c) characterizes the force (61) for being physically meaningful. It *preserves the elastic properties* in uncracked zones.

3.1.6. Qualitative features of different driving forces

Though crack propagation is a highly inhomogeneous phenomenon and should be only considered in the multi-dimensional context, a look at homogeneous and one-dimensional states in Figs. 4 and 5 may illustrate the modeling capabilities. For *homogeneous states* with zero Laplacian $\Delta d = 0$, Eq. (19) has the closed-form solution

$$d(t) = \frac{\mathcal{H}(t)}{1 + \mathcal{H}(t)} \quad \text{with} \quad \mathcal{H}(t) := \max_{s\in[0,t]} \tilde{D}(s) \tag{63}$$

with start value $d(0) = 0$ for a virgin state $\tilde{D}(0) = 0$. Note the limit $d \to 1$ for $\mathcal{H} \to \infty$. As depicted in Fig. 4, the length-scale l controls the shape of the fracture phase field d that turns out to be jump-like for $l \to \infty$. Assuming for the qualitative description in Figs. 4 and 5 the quadratic effective energy functions

$$\tilde{\psi} = \frac{E}{2}\varepsilon^2 \quad \text{and} \quad \tilde{\psi}^* = \frac{1}{2E}\tilde{\sigma}^2 \tag{64}$$

in the *small strain context*, the stress function is postulated to have the form

$$\sigma = (1-d)^2\tilde{\sigma} \quad \text{with } \tilde{\sigma} = E\varepsilon. \tag{65}$$

The phase field is computed by the above closed-form result. The *energetic driving force without threshold* (49) takes the form

$$\tilde{D}_1 = \frac{2\tilde{\psi}}{g_c/l} = \frac{E\varepsilon^2}{g_c/l} \quad \text{or} \quad \tilde{D}_1 = \frac{2\tilde{\psi}^*}{g_c/l} = \frac{\tilde{\sigma}^2/E}{g_c/l}, \tag{66}$$

alternatively in terms of the strains ε or the effective stresses $\tilde{\sigma}$. As shown in Fig. 4(a) the stress σ defined in (65) has for a given *critical energy release rate* g_c different peak values

$$\sigma_c = \frac{9}{16} E\varepsilon_c \quad \text{with } \varepsilon_c = \sqrt{\frac{g_c/l}{3E}}, \tag{67}$$

which depend on the length scale l. This has been pointed out by Borden et al. [3]. A modification of (66) that uses the *critical fracture stress* σ_c as a material parameter resolves $(67)_1$ for a length-scale-dependent g_c

$$\hat{g}_c(l) = \frac{256}{27}\frac{\sigma_c^2 l}{E}, \tag{68}$$

yielding driving forces which do not depend on the length scale l

$$\tilde{D}_1 = \frac{27}{256}\Big(\frac{E\varepsilon}{\sigma_c}\Big)^2 \quad \text{or} \quad \tilde{D}_1 = \frac{27}{256}\Big(\frac{\tilde{\sigma}}{\sigma_c}\Big)^2. \tag{69}$$

Fig. 4(b) shows that such a setting gives a homogeneous stress response σ independent of the length scale l. This is also the case for the *energetic driving force with threshold* (54) that takes the form

$$\tilde{D}_2 = \zeta\Big\langle \frac{\tilde{\psi}}{\psi_c} - 1\Big\rangle = \zeta\Big\langle \Big(\frac{\varepsilon}{\varepsilon_c}\Big)^2 - 1\Big\rangle \quad \text{or} \quad \tilde{D}_2 = \zeta\Big\langle \frac{\tilde{\psi}^*}{\psi_c^*} - 1\Big\rangle = \zeta\Big\langle \Big(\frac{\tilde{\sigma}}{\sigma_c}\Big)^2 - 1\Big\rangle \tag{70}$$

alternatively in terms of tensile strains ε or the effective tensile stresses $\tilde{\sigma}$. Here, the energetic threshold was expressed by $\psi_c := E\varepsilon_c^2/2$ or $\psi_c^* := \tilde{\sigma}_c^2/2E$ by strain and stress thresholds ε_c and σ_c, respectively. Note that response of the $\tilde{D}_2$ shown in Fig. 4(c) is independent of the length scale l. Fig. 5 depicts the simulation of cracking in a one-dimensional bar, with a slight perturbation of the fracture toughness in its center. In contrast to the energetic criterion $\tilde{D}_1$ in Figs. 5(a)–(b), the maximum stress criterion $\tilde{D}_2$ in Fig. 5(c) does not affect zones in a far distance of the crack. The solution *converges* for $l \to 0$ to a sharp crack discontinuity. This is a strong argument for the criterion (61) with threshold.

3.2. Transition rules from unbroken to fully broken response

Depending on the crack phase field $d \in [0, 1]$, constitutive functions for the *degrading elastic solid response* as well as the growth of *new non-mechanical effects in damaged zones* need to be constructed, which account for the specific multi-physics scenario under consideration. The first set of functions concern the degradation of elastic stored energy, stresses and non-mechanical fluxes in the solid with increasing phase field d. The second set of functions describes a new constitutive response in the damaged domain that raises with increasing phase field d, e.g. the modeling of non-mechanical fluxes such as heat flow, diffusion, electric displacements or magnetic induction across diffusive crack faces. In order to set up a general structure for the transition from the unbroken to the fully broken response, consider a *generic constitutive function*

$$\boldsymbol{f} = \hat{\boldsymbol{f}}(state; d), \tag{71}$$

where only the fracture phase field d is specified and *state* stands for a *set of constitutive state variables*, e.g. those in Section 4 for the case of thermo-elasticity. The above mentioned degrading and growth responses in the range $d \in [0, 1]$ of the crack phase field may be described by a *transition rule*, which assumes the constitutive structure

$$\hat{\boldsymbol{f}}(state; d) = \hat{\boldsymbol{f}}^s(state; d) + \hat{\boldsymbol{f}}^c(state; d) \tag{72}$$

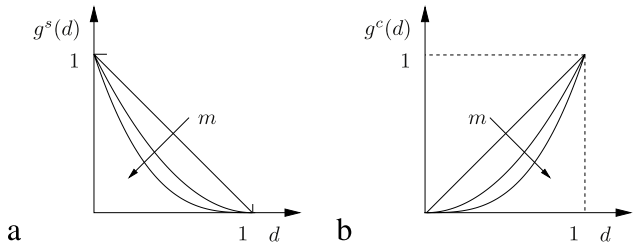

Fig. 7. (a) Fracture degradation function for solid response $g^s(d) = (1-d)^m$ with $m = \{1, 2, 3\}$ and (b) build up function for diffusive crack phase $g^c(d) = d^m$ with $m = \{1, 2, 3\}$.

with degrading functions $\hat{\boldsymbol{f}}^s$ for the solid response and growing functions $\hat{\boldsymbol{f}}^c$ in diffusive crack zones. These functions are related to *effective functions*

$$\tilde{\boldsymbol{f}}^s(state) := \hat{\boldsymbol{f}}^s(state; 0) \quad \text{and} \quad \tilde{\boldsymbol{f}}^c(state) := \hat{\boldsymbol{f}}^c(state; 1) \tag{73}$$

which describe the responses at fully unbroken and fully broken states, respectively. The character of de- and increasing functions is defined by the properties

$$\partial_d \hat{\boldsymbol{f}}^s(state; d) \leq \boldsymbol{0} \wedge \hat{\boldsymbol{f}}^s(state; 1) = \boldsymbol{0} \quad \text{and} \quad \hat{\boldsymbol{f}}^c(state; 0) = \boldsymbol{0} \wedge \partial_d \hat{\boldsymbol{f}}^c(state; d) \geq \boldsymbol{0}. \tag{74}$$

A simple constitutive assumption for the transition rule (72) is the ansatz

$$\boxed{\hat{\boldsymbol{f}}(state; d) = g^s(d)\tilde{\boldsymbol{f}}^s(state) + g^c(d)\tilde{\boldsymbol{f}}^c(state)} \tag{75}$$

where $\tilde{\boldsymbol{f}}^s$ and $\tilde{\boldsymbol{f}}^c$ are the functions defined in (73). The weight functions for the unbroken and fully broken phases are assumed to be continuous, satisfying the conditions

$$\begin{matrix} g^{s\prime}(d) \leq 0, \\ g^{c\prime}(d) \geq 0, \end{matrix} \quad \text{with} \quad \begin{matrix} g^s(0) = 1, \\ g^c(0) = 0, \end{matrix} \quad \text{and} \quad \begin{matrix} g^s(1) = 0, \\ g^c(1) = 1. \end{matrix} \tag{76}$$

A simple example are the functions $g^s(d) = (1-d)^m$ with dual $g^c(d) = d^m$ depicted in Fig. 7, where $g^s(d)$ recovers for $m = 1$ the classical $(1-d)$-theory of damage and for $m = 2$ the ansatz (43) of the variational theory of brittle fracture in elastic solids outlined in Miehe et al. [1]. A quadratically increasing function $g^c(d) = d^2$ for the diffusive crack zone can be motivated for a heat transfer across crack faces based on geometric arguments, i.e. consistent with the crack surface density function $\gamma_l(d, \nabla d)$ defined in (9), see Section 5 for further details.

4. Finite thermoelasticity coupled with phase field fracture

Having the modular phase field concept for the evolution of a crack surfaces at hand, this section combines it with the modeling of a multi-physics bulk response. In this context, the phase field d enters the constitutive functions as a generalized internal variable. However, it is considered as a geometric property that models a regularized crack surface.

4.1. Primary fields of thermoelasticity and their gradients

The boundary-value-problem for the modeling of thermomechanical problems in solids is a coupled problem, characterized by the *deformation field* of the solid and the absolute *temperature field* shown in Fig. 8

$$\boldsymbol{\varphi} : \begin{cases} \mathcal{B}_0 \times \mathcal{T} \to \mathcal{B}_t \subset \mathcal{R}^3 \\ (\boldsymbol{X}, t) \mapsto \boldsymbol{x} = \boldsymbol{\varphi}(\boldsymbol{X}, t) \end{cases} \quad \text{and} \quad \theta : \begin{cases} \mathcal{B}_0 \times \mathcal{T} \to \mathcal{R}_+ \\ (\boldsymbol{X}, t) \mapsto \theta(\boldsymbol{X}, t) \end{cases} . \tag{77}$$

As visualized in Fig. 1, the deformation field $\boldsymbol{\varphi}$ maps at time $t \in \mathcal{T}$ points $\boldsymbol{X} \in \mathcal{B}_0$ of the reference configuration $\mathcal{B}_0 \subset \mathcal{R}^3$ onto points $\boldsymbol{x} \in \mathcal{B}_t$ of the current configuration $\mathcal{B}_t \subset \mathcal{R}^3$. The gradients of these fields define the *material*

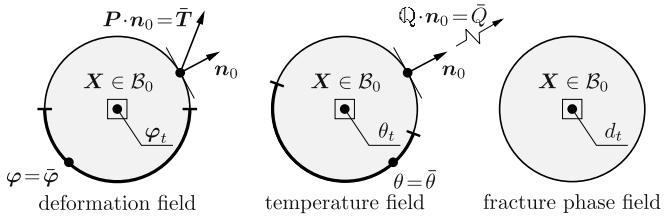

Fig. 8. Primary fields in thermo-elasticity coupled with phase field fracture. The deformation field $\boldsymbol{\varphi}$, temperature field θ and phase field d are defined on the solid domain $\mathcal{B}_0$. The boundary $\partial\mathcal{B}_0$ of the solid is decomposed for Dirichlet- and Neumann-type boundary conditions associated with the mechanical and thermal problem. The diffusive fracture problem has zero Neumann conditions on the full boundary.

deformation gradient and the *material temperature gradient*

$$\boxed{\boldsymbol{F} := \nabla\boldsymbol{\varphi} \quad \text{and} \quad \mathbb{F} := \nabla\theta} \tag{78}$$

respectively. The deformation gradient $\boldsymbol{F}$ itself, its cofactor $\text{cof}[\boldsymbol{F}] = \det[\boldsymbol{F}]\boldsymbol{F}^{-T}$ and its Jacobian $J := \det[\boldsymbol{F}]$ characterize the deformation of infinitesimal line, area and volume elements

$$d\boldsymbol{x} = \boldsymbol{F}d\boldsymbol{X}, \qquad d\boldsymbol{a} = \text{cof}[\boldsymbol{F}]d\boldsymbol{A}, \qquad dv = \det[\boldsymbol{F}]dV. \tag{79}$$

The map $\boldsymbol{\varphi}$ is constrained by the condition $J := \det[\boldsymbol{F}] > 0$ in order to ensure non-penetrable deformations. Furthermore, let $\boldsymbol{g}, \boldsymbol{G} \in Sym_+(3)$ be the standard metrics of the current and reference configurations $\mathcal{B}_0$ and $\mathcal{B}_t$. Then

$$\boldsymbol{C} := \boldsymbol{F}^T\boldsymbol{g}\boldsymbol{F} \quad \text{and} \quad \boldsymbol{c} := \boldsymbol{F}^{-T}\boldsymbol{G}\boldsymbol{F}^{-1} \tag{80}$$

are convected current and reference metrics, often denoted as the *right and left Cauchy–Green tensors*, respectively. They define Green's and Almansi's strain tensors

$$\boldsymbol{E} := \frac{1}{2}[\boldsymbol{C} - \boldsymbol{G}] \quad \text{and} \quad \boldsymbol{\varepsilon} := \frac{1}{2}[\boldsymbol{g} - \boldsymbol{c}], \tag{81}$$

respectively. The *spatial temperature gradient* is obtained by a parametrization of the temperature by the spatial coordinates $\boldsymbol{x} = \boldsymbol{\varphi}(\boldsymbol{X}, t)$, yielding the relationship

$$\mathbb{f} := \nabla_{\boldsymbol{x}}\theta(\boldsymbol{x}, t) = \boldsymbol{F}^{-T}\mathbb{F}. \tag{82}$$

4.2. Stress tensors and heat flux vectors

4.2.1. Stress tensors

Consider a part $\mathcal{P}_0 \subset \mathcal{B}_0$ cut out of the reference configuration $\mathcal{B}_0$ and its spatial counterpart $\mathcal{P}_t \subset \mathcal{B}_t$, with boundaries $\partial\mathcal{P}_0$ and $\partial\mathcal{P}_t$, respectively. The total stress vector $\boldsymbol{t}$ acts on the surface element $d\boldsymbol{a} \subset \partial\mathcal{P}_t$ on the deformed configuration and represents the force that the rest of the body $\mathcal{B}_t \setminus \mathcal{P}_t$ exerts on $\mathcal{P}_t$ through $\partial\mathcal{P}_t$. Cauchy's stress theorem defines the traction to depend linearly on the outward surface normal

$$\boldsymbol{t}(\boldsymbol{x}, t; \boldsymbol{n}) := \boldsymbol{\sigma}(\boldsymbol{x}, t) \cdot \boldsymbol{n} \tag{83}$$

through the *total Cauchy stress tensor* $\boldsymbol{\sigma}$. Now consider the identity $\boldsymbol{T}dA = \boldsymbol{t}da$ by scaling the (true) spatial force $\boldsymbol{t}da$ by the reference area element dA. This induces the definition of the *nominal stress tensor* $\boldsymbol{P}$ by setting

$$\boldsymbol{P} \cdot d\boldsymbol{A} = \boldsymbol{\sigma} \cdot d\boldsymbol{a} \quad \text{with } \boldsymbol{P} := (J\boldsymbol{\sigma})\boldsymbol{F}^{-T}, \tag{84}$$

where the area map $(79)_2$ was inserted. Here, $\boldsymbol{\tau} := J\boldsymbol{\sigma}$ is denoted as the total *Kirchhoff stress* and $\boldsymbol{S} := \boldsymbol{F}^{-1}\boldsymbol{\tau}\boldsymbol{F}^{-T}$ as the *symmetric Lagrangian stress*.

4.2.2. Heat flux vectors

Consider a heat out-flux q through the surface element $d\boldsymbol{a}$ of $\partial\mathcal{P}_t$ in the current configuration, that depends linearly on the outward normal

$$q(\boldsymbol{x}, t; \boldsymbol{n}) := \mathfrak{q}(\boldsymbol{x}, t) \cdot \boldsymbol{n} \tag{85}$$

through the *spatial heat flux vector* $\mathfrak{q}$. A modified heat flux Q is then defined by the identity $QdA = qda$. This induces the definition of the *material heat flux* by setting

$$\mathbb{Q} \cdot d\boldsymbol{A} = \mathfrak{q} \cdot d\boldsymbol{a} \quad \text{with } \mathbb{Q} := \boldsymbol{F}^{-1}(J\mathfrak{q}), \tag{86}$$

where we made use of the area map $(79)_2$. $\mathbb{h} := J\mathfrak{q}$ is the *Kirchhoff-type heat flux*.

4.3. General equations of finite thermo-elasticity

4.3.1. Global equations

The general equations which drive the coupled thermomechanical problem are formulated as balances for a part $\mathcal{P}_t \subset \mathcal{B}_t$ of the deformed configuration. The *conservation of mass* reads

$$\int_{\mathcal{P}_t} \rho \, dv = \int_{\mathcal{P}_0} \rho_0 \, dV, \tag{87}$$

where $\rho(\boldsymbol{x}, t)$ and $\rho_0(\boldsymbol{X})$ are the density fields of the current and the reference configurations, respectively. The *conservations of linear momentum* is

$$\frac{d}{dt} \int_{\mathcal{P}_t} \rho \boldsymbol{v} \, dv = \int_{\partial\mathcal{P}_t} \boldsymbol{t} \, da + \int_{\mathcal{P}_t} \rho \boldsymbol{\gamma} \, dv, \tag{88}$$

and the *conservations of angular momentum* states

$$\frac{d}{dt} \int_{\mathcal{P}_t} \boldsymbol{x} \times \rho \boldsymbol{v} \, dv = \int_{\partial\mathcal{P}_t} \boldsymbol{x} \times \boldsymbol{t} \, da + \int_{\mathcal{P}_t} \boldsymbol{x} \times \rho \boldsymbol{\gamma} \, dv, \tag{89}$$

where $\boldsymbol{v} := \dot{\boldsymbol{\varphi}} \circ \boldsymbol{\varphi}^{-1}$ is the spatial velocity field. $\boldsymbol{\gamma}(\boldsymbol{x}, t)$ is a given body force field. Finally, the *conservation of energy* of the part $\mathcal{P}_t \subset \mathcal{B}_t$ takes the form

$$\frac{d}{dt} \int_{\mathcal{P}_t} \rho \Big[e + \frac{1}{2}|\boldsymbol{v}|^2 \Big] dv = \int_{\partial\mathcal{P}_t} [\boldsymbol{t} \cdot \boldsymbol{v} - q] \, da + \int_{\mathcal{P}_t} [\rho \boldsymbol{\gamma} \cdot \boldsymbol{v} + \rho r] \, dv, \tag{90}$$

where e is the stored internal energy and r is the given heat source. In addition to these global balances of thermoelasticity, the global *balance of the regularized crack surface* (13) governs the fracture phase field d.

4.3.2. Local equations

Pulling back these integrals to the reference configuration by using the volume map $(79)_3$, inserting the definitions (83)–(86) for the traction $\boldsymbol{t}$ and the heat out-flux q, using the Gauss theorem and the standard localization argument, we end up with *four balance equations*

1.	Balance of mass	$\rho_0 = \rho J$
2.	Balance linear momentum	$\rho_0 \ddot{\boldsymbol{\varphi}} = \mathrm{Div}[\boldsymbol{P}] + \rho_0 \boldsymbol{\gamma}$
3.	Balance angular momentum	$\mathrm{skew}[\boldsymbol{P}\boldsymbol{F}^T] = \boldsymbol{0}$
4.	Balance internal energy	$\rho_0 \dot{e} = \boldsymbol{P} : \dot{\boldsymbol{F}} - \mathrm{Div}[\mathbb{Q}] + \rho_0 r$
5.	Constitutive stresses	$\boldsymbol{P} = \rho_0 \partial_{\boldsymbol{F}} \hat{\Psi}(\boldsymbol{C}, \theta; d, \boldsymbol{X})$
6.	Constitutive entropy	$\eta = -\partial_\theta \hat{\Psi}(\boldsymbol{C}, \theta; d, \boldsymbol{X})$
7.	Constitutive heat flux	$\mathbb{Q} = \partial_{\mathbb{G}} \hat{\Phi}(\mathbb{G}; \boldsymbol{C}, \theta, d, \boldsymbol{X})$

(91)

defined on the reference configuration $\mathcal{B}_0$. Recall in this context the Piola transformations $\mathrm{Div}[\mathbb{Q}] = J\,\mathrm{div}_{\boldsymbol{x}}[\mathbb{h}/J]$ and $\mathrm{Div}[\boldsymbol{P}] = J\,\mathrm{div}_{\boldsymbol{x}}[\boldsymbol{\tau}/J]$, which allow to express the above material divergence terms as spatial divergence terms of the Kirchhoff-type heat flux $\mathbb{h} := J\mathbb{q}$ and the Kirchhoff stress tensor $\boldsymbol{\tau} := J\boldsymbol{\sigma}$. Furthermore, note that the third equation simply states the symmetry of the Cauchy stress $\boldsymbol{\sigma}$. In addition, as summarized in Box II, the local equation (19) governs the fracture phase field d.

4.4. Principle of irreversibility and constitutive equations

4.4.1. Dissipation principle

The formulation of the constitutive equations must be consistent with a principle of irreversibility, i.e. the second axiom of thermodynamics. This is expressed by the *global dissipation postulate*

$$\frac{d}{dt}\int_{\mathcal{P}_t}\rho\eta\,dv \geq -\int_{\partial\mathcal{P}_t}\frac{q}{\theta}\,da + \int_{\mathcal{P}_t}\rho\frac{r}{\theta}\,dv, \tag{92}$$

where η is the entropy density. Pulling back these integrals to the reference configuration with the volume map $(79)_3$, inserting the definitions (85)–(86) for the heat out-flux q, using the Gauss theorem, the standard localization argument and inserting the balance equations (91) give the *local dissipation postulate*

$$\rho_0\mathcal{D} := \boldsymbol{P} : \dot{\boldsymbol{F}} - \rho_0\eta\dot{\theta} - \rho_0\,\dot{\Psi} - \frac{1}{\theta}\mathbb{Q}\cdot\nabla\theta \geq 0, \tag{93}$$

known as the *Clausius–Duhem inequality*. Here, we eliminated the internal energy based on the Legendre transformation

$$e = \Psi + \theta\eta, \tag{94}$$

where Ψ is the free Helmholtz energy. This equation can be split up into a part due to local actions and a part due to heat conduction

$$\rho_0\mathcal{D}_{loc} := \boldsymbol{P} : \dot{\boldsymbol{F}} - \rho_0\eta\dot{\theta} - \rho_0\,\dot{\Psi} \geq 0 \quad \text{and} \quad \rho_0\mathcal{D}_{con} := \mathbb{Q}\cdot\mathbb{G} \geq 0, \tag{95}$$

where $\mathbb{G}$ is the driving force dual to the heat flux $\mathbb{Q}$, with spatial counterpart $\mathbb{g}$, i.e.

$$\mathbb{G} := -\frac{1}{\theta}\nabla\theta \quad \text{and} \quad \mathbb{g} := -\frac{1}{\theta}\nabla_{\boldsymbol{x}}\theta = \boldsymbol{F}^{-T}\mathbb{G} \tag{96}$$

in analogy to (82).

4.4.2. Objective free energy function

The constitutive equations are constructed such that the above dissipation conditions (93) are a priori satisfied for all processes. Assuming a local theory of the grade one, the free energy is assumed to depend on the primary variables (77) and its first gradients

$$\Psi = \hat{\Psi}(\boldsymbol{\varphi}, \nabla\boldsymbol{\varphi}, \theta, \nabla\theta; d, \boldsymbol{X}). \tag{97}$$

In addition, the free energy function *depends on the fracture phase field* d, as already pointed out in (71)–(76) and Box I. However, as indicated by the semicolon, this dependence is considered as a *geometric property in the sense of a regularized crack discontinuity*. The dependence of $\hat{\Psi}$ on the phase field d models the degradation of the bulk energy density. Note that we do not use a "total" pseudo-energy of the form W in (51), that contains an additional surface energy contribution. Such a function is often included in mathematical structure of pure mechanical models. However, in the non-isothermal context presented here, where the quantification of energy and the dissipation is important, a storage of surface energy during fracture seems not appropriate. Instead, we view the *fracture process as a fully dissipative phenomenon* where the degrading bulk energy is fully converted into heat. As a consequence, the crack surface density function γ_l defined in (8) in terms of ∇d does not enter the bulk energy density $\hat{\Psi}$. It simply describes the crack resistance but not an energy storage. The description of the degradation of the bulk energy density $\hat{\Psi}$ does not need a dependence on the gradient ∇d of the phase field.

Demanding invariance of $\hat{\Psi}$ with respect to rigid deformation superimposed on the current configuration $\boldsymbol{\varphi}^+ = \boldsymbol{Q}\boldsymbol{\varphi} + \boldsymbol{c}$ for all translations $\boldsymbol{c}(t)$ and rotations $\boldsymbol{Q}(t) \in SO(3)$, as well as consistency with the dissipation principle (93), we obtain the reduced form

$$\boxed{\Psi = \hat{\Psi}(\boldsymbol{F}, \theta; d, \boldsymbol{X}) = \bar{\Psi}(\boldsymbol{C}, \theta; d, \boldsymbol{X})} \tag{98}$$

in terms of the right Cauchy–Green tensor $\boldsymbol{C}$ defined in (80). Insertion into $(95)_1$ then gives the constitutive equations $(91)_{5–6}$ consistent with the dissipation principle (92). The local dissipation $(95)_1$ then attains the reduced form

$$\rho_0 \mathcal{D}_{loc} = \mathfrak{D}\dot{d} \geq 0 \quad \text{with } \mathfrak{D} := -\rho_0 \partial_d \hat{\Psi}(\boldsymbol{C}, \theta; d, \boldsymbol{X}). \tag{99}$$

Here, $\mathfrak{D}$ is the energetic dual variable to the fracture phase field d. Note that this thermodynamic constraint is ensured by modeling a positive force $\mathfrak{D} \geq 0$ and the assumed growth condition $(24)_2$ of the crack phase field.

4.4.3. Objective and convex dissipation potential

In order to prescribe the heat flux in the bulk, we define an objective dissipation potential that depends on the driving force $\mathbb{G}$ defined in (96), i.e.

$$\boxed{\Phi = \hat{\Phi}(\mathbb{G}; \boldsymbol{F}, \theta, d, \boldsymbol{X}) = \bar{\Phi}(\mathbb{G}; \boldsymbol{C}, \theta, d, \boldsymbol{X})} \tag{100}$$

at a *given* state $\{\boldsymbol{F}, \theta, d\}$ of deformation, temperature and crack phase field. The heat flux dissipation potential function depends on the fracture phase field d by a transition rule as pointed out in (71)–(76). Then the heat flux vector $\mathbb{Q}$ is defined by the constitutive equation $(91)_7$. The dissipation inequality $(95)_2$ is satisfied if $\hat{\Phi}$ is a *convex function* with respect to the heat flux driving force $\mathbb{G}$.

4.5. The temperature evolution equation

Based on the Legendre transformation (94), we obtain by insertion of the constitutive equations $(91)_{5–6}$ the evolution $\rho_0 \dot{e} = \boldsymbol{P} : \dot{\boldsymbol{F}} + \rho_0 \theta \dot{\eta} - \rho_0 \mathcal{D}_{loc}$. Insertion into $(91)_4$ gives the evolution equation for the entropy

$$\rho_0 \theta \dot{\eta} = -\mathrm{Div}[\mathbb{Q}] + \rho_0 (r + \mathcal{D}_{loc}). \tag{101}$$

Starting from $(91)_6$, we obtain the constitutive rate equation $\rho_0 \theta \dot{\eta} = \rho_0 c \dot{\theta} - \rho_0 \mathcal{L}$ with the *heat capacity* and the *latent heating*

$$c := -\theta \partial^2_{\theta\theta} \hat{\Psi} \quad \text{and} \quad \mathcal{L} := \theta \partial^2_{\boldsymbol{F}\theta} \hat{\Psi} : \dot{\boldsymbol{F}} + \theta \partial^2_{d\theta} \hat{\Psi} \cdot \dot{d}. \tag{102}$$

Insertion into (101) finally gives an evolution equation for the temperature

$$\rho_0 c \dot{\theta} = -\mathrm{Div}[\mathbb{Q}] + \rho_0 [r + \mathcal{L} + \mathcal{D}_{loc}]. \tag{103}$$

Note that we have for adiabatic processes $\mathbb{Q} \equiv \boldsymbol{0}$ and $r \equiv 0$. Eq. (103) is the coupled temperature evolution equation of thermoelasticity coupled with latent and dissipative heating effects due to fracture.

4.6. The boundary conditions for the coupled problem

In order to be able to solve the system of Eqs. (91) for finite thermoelasticity coupled with the fracture phase field equation (19), we have to postulate boundary conditions for the coupled problem. To this end, the surface $\partial\mathcal{B}_0$ of the reference configuration is decomposed into mechanical and thermal parts

$$\partial\mathcal{B}_0 = \partial\mathcal{B}_0^{\varphi} \cup \partial\mathcal{B}_0^{t} \quad \text{and} \quad \partial\mathcal{B}_0 = \partial\mathcal{B}_0^{\theta} \cup \partial\mathcal{B}_0^{q}, \tag{104}$$

respectively, with $\partial\mathcal{B}_0^{\varphi} \cap \partial\mathcal{B}_0^{t} = \emptyset$ and $\partial\mathcal{B}_0^{\theta} \cap \partial\mathcal{B}_0^{q} = \emptyset$. We postulate Dirichlet- and Neumann-type boundary conditions for the mechanical problem

$$\boldsymbol{\varphi} = \bar{\boldsymbol{\varphi}}(\boldsymbol{X}, t) \quad \text{on } \partial\mathcal{B}_0^{\varphi} \quad \text{and} \quad \boldsymbol{\sigma} \cdot \boldsymbol{n} = \bar{\boldsymbol{t}}(\boldsymbol{x}, t) \quad \text{on } \partial\mathcal{B}_t^{t}, \tag{105}$$

and for the thermal problem

$$\theta = \bar{\theta}(\boldsymbol{X}, t) \quad \text{on } \partial\mathcal{B}_0^\theta \quad \text{and} \quad \mathbb{q} \cdot \boldsymbol{n} = \bar{q}(\boldsymbol{x}, t) \quad \text{on } \partial\mathcal{B}_t^q, \tag{106}$$

with *prescribed* deformation $\bar{\boldsymbol{\varphi}}$, traction $\bar{\boldsymbol{t}}$, temperature $\bar{\theta}$ and heat out-flux $\bar{q}$, respectively. Of particular importance is the *convective heat exchange*, governed by the constitutive equation

$$\bar{q}_C = h_C(\theta - \theta_\infty) \quad \text{on } \partial\mathcal{B}_t^q \tag{107}$$

defined on the exterior boundary, where h_C is the convective heat exchange coefficient and θ_∞ a given ambient temperature. In addition to the above conditions, the homogeneous Neumann-type boundary conditions (20) are applied for the fracture phase field d.

5. Constitutive functions for the bulk response

This sections specifies constitutive functions and for the free energy and the heat flux dissipation potential for a model problem of thermoelasticity at fracture.

5.1. The free energy storage function

The energy storage function introduced in (98) decomposes into a part due to *elastic distortions* and a purely *thermal part*

$$\boxed{\hat{\Psi}(\mathit{state}; d) = (1-d)^2\, \tilde{\Psi}_e(\boldsymbol{F}^e(\boldsymbol{F}, \theta)) + \tilde{\Psi}_\theta(\theta)}. \tag{108}$$

The *elastic contribution* is assumed to be of a compressible neo-Hookean form

$$\rho_0\, \tilde{\Psi}_e(\boldsymbol{F}^e) = \frac{\mu}{2}[\boldsymbol{F}^e : \boldsymbol{F}^e - 3] + \frac{\mu}{\beta}[(\det \boldsymbol{F}^e)^{-\beta} - 1], \tag{109}$$

formulated in terms of the elastic, stress-producing deformation

$$\boldsymbol{F}_e = J_\theta^{-1/3} \boldsymbol{F} \quad \text{with } J_\theta = \exp[3\alpha(\theta - \theta_0)] \tag{110}$$

that is a function of the volumetric thermal expansion J_θ that depends on the temperature θ. The multiplicative split $\boldsymbol{F} = \boldsymbol{F}_e \boldsymbol{F}_\theta$ of the deformation gradient into a volumetric thermal part $\boldsymbol{F}_\theta := J_\theta^{-1/3} \boldsymbol{1}$ and an elastic part $\boldsymbol{F}_e$ is in line with treatments in Lu and Pister [41]. $\mu > 0$ is the shear modulus and the parameter $\beta > 0$ describes a weak volumetric compressibility of the material, and can be linked to the classical Poisson ratio of linear elasticity via $\beta = 2\nu/1 - 2\nu$. The purely *thermal contribution* to the stored energy (108) is assumed to have the simple form

$$\rho_0\, \tilde{\Psi}_\theta(\theta) = -\rho_0 c \Big[\theta \ln \frac{\theta}{\theta_0} - (\theta - \theta_0)\Big], \tag{111}$$

where c is a heat capacity parameter that is assumed to be a constant. A *degradation due to fracture* by the function $g^s(d) = (1-d)^2$ is assumed for the full elastic energy storage.

5.2. Heat flux dissipation potential function

The dissipation potential that characterizes the heat flow introduced in (100) depends on driving force $\mathbb{G} := -\nabla\theta/\theta$ introduced in (96). It is assumed to have the convex quadratic form

$$\boxed{\hat{\Phi}_{con}(\mathbb{G}; \boldsymbol{F}, \theta, d) = \hat{k}(d) \boldsymbol{C}^{-1} : (\mathbb{G} \otimes \mathbb{G})/2} \tag{112}$$

that models a transport law based on the *spatial gradient* of the temperature. The function $\hat{k} \geq 0$ is the thermal conductivity, that is assumed to degrade in the case of fracture by the transition

$$\hat{k}(d) = (1-d)^2 k^s + d^2 k^c \tag{113}$$

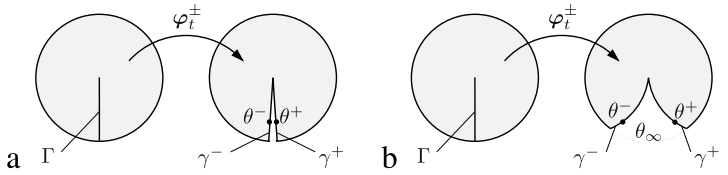

Fig. 9. Thermal boundary conditions on sharp crack faces, which are treated in the continuum phase field formulation in a regularized manner. (a) *Conduction across gap* for moderate crack opening with heat transport $q_T = -h_T(\theta^+ - \theta^-)$. (b) *Convective heat exchange* for large crack opening with heat source $q_C^{\pm} = h_C(\theta^+ - \theta^-)$.

governed by the parameters $k^s \geq$ and $k^c \geq 0$. The transition rule (113) with the quadratic growth term is motivated in Section 5.4.

5.3. The derived constitutive functions

With the above two functions (108) and (112), an evaluation of the constitutive expressions $(91)_{5-7}$ gives the derived constitutive functions

$$\begin{aligned} \boldsymbol{P} &= (1-d)^2 \mu J_\theta^{-1/3}[\boldsymbol{F}^e - J_e^{-\beta}\boldsymbol{F}^{e-T}], \\ \eta &= c\ln(\theta/\theta_0) + 3\alpha J_\theta^{-1} p \quad \text{with } p := -\frac{1}{3}\mathrm{tr}[\boldsymbol{P}\boldsymbol{F}^T], \\ \mathbb{Q} &= -\big[(1-d)^2 k^s + d^2 k^c\big]\boldsymbol{C}^{-1}\nabla\theta/\theta, \end{aligned} \tag{114}$$

for the first Piola stress, the entropy and the material heat flux.

5.4. Heat conduction across crack faces

The appearance of a *heat conduction* though the medium enclosed by the crack faces needs the construction of a constitutive function in the damaged zones as already considered in (72). In order to motivate a constitutive equation (113) for the heat flux across crack faces, consider a *transition from the sharp crack modeling to the phase field modeling*. Fig. 9 shows a sharp crack. Let Γ denote the sharp crack surface, and $\gamma^{\pm} = \boldsymbol{\varphi}_t^{\pm}(\Gamma)$ the deformed crack faces. Assume that the deformed crack surfaces $\gamma^{\pm}$ stay close to each other, and consider the simple constitutive equations

$$q_T = -h_T[\![\theta]\!] \quad \text{on } \boldsymbol{\varphi}_t^{\pm}(\Gamma) \tag{115}$$

for the heat transport across the crack, where $[\![\theta]\!] := \theta^+ - \theta^-$ is the temperature jump. $\theta^{\pm}$ are the temperatures at the crack faces $\gamma^{\pm}$ and h_T a *heat transition parameter*. Hence, the transport of heat across a sharp crack surface is

$$T^c := \int_{\boldsymbol{\varphi}_t^-(\Gamma)} q_T\, da = -\int_\Gamma l_{\boldsymbol{x}} h_T \frac{[\![\theta]\!]}{l_{\boldsymbol{x}}}\, da \tag{116}$$

where $l_{\boldsymbol{x}}$ is a characteristic length. A transition of this sharp crack setting to the regularized phase field formulation is achieved by the transition of the material crack surface element $dA \to \gamma_l(d;\nabla d)dV$ towards the volume element, governed by the crack surface density function $\gamma_l(d;\nabla d)$ defined in (9). Furthermore, the spatial gradient in (116) may be replaced by the continuum gradient normal to the crack, i.e. $[\![\theta]\!]/l_{\boldsymbol{x}} \to \nabla_{\boldsymbol{x}}\theta \cdot \boldsymbol{n}$, where $\boldsymbol{n}$ is the normal to the crack surface $\boldsymbol{\varphi}(\Gamma)$. Taking into account the geometric relationships $\nabla_{\boldsymbol{x}}\theta = \boldsymbol{F}^{-T}\nabla\theta$, $dv = \det[\boldsymbol{F}]dV$ and $\boldsymbol{n}da = \det[\boldsymbol{F}]\boldsymbol{F}^{-T}\boldsymbol{n}_0 dA$, we obtain the continuum approximation

$$T^c \approx T_l^c := -\int_{\mathcal{B}} l_{\boldsymbol{x}} h_T(\boldsymbol{C}^{-1}\nabla\theta\cdot\boldsymbol{n}_0)\gamma_l(d;\nabla d)\, dv = \int_{\mathcal{B}} \mathfrak{Q}^c \cdot \boldsymbol{n}_0\, dv \tag{117}$$

of the transport (116), where

$$\mathfrak{Q}^c := -l_{\boldsymbol{x}} h_T \boldsymbol{C}^{-1}\nabla\theta\gamma_l(d;\nabla d) = -l_{\boldsymbol{x}} h_T \boldsymbol{C}^{-1}\nabla\theta\frac{1}{2l}\big[d^2 + l^2|\nabla d|^2\big] \tag{118}$$

is a *heat flux per unit volume* across the damaged zone. Assuming both terms in the bracket of the same order, which is true for a damage profile of the form $d(x) = \exp[-|x|/l]$ in terms of a scalar coordinate x perpendicular to the crack, a *material heat flux per area* is estimated to have the constitutive form

$$\boxed{\mathbb{Q}^c \approx l\mathfrak{Q}^c = -l_{\boldsymbol{x}} h_T d^2 \boldsymbol{C}^{-1}\nabla\theta}. \tag{119}$$

Note that the growth function $g^c(d) = d^2$ models in the range $d \in [0, 1]$ a quadratic increase of the heat transport across a regularized crack that motivates the ansatz (113) by the relation

$$k^c \approx l_{\boldsymbol{x}} h_T. \tag{120}$$

Hence, in the phase field modeling of fracture, a reduced heat conductivity in the damaged zone models a heat transfer across nearby crack faces as visualized in Fig. 9(a).

5.5. Convective heat exchange at crack faces

The appearance of a possible *convective heat exchange* at a free crack surface can be modeled in the continuum phase field modeling of fracture by an additional heat source. In order to motivate this, assume that the deformed crack surfaces $\gamma^{\pm} = \boldsymbol{\varphi}_t^{\pm}(\Gamma)$ are in contact with an ambient temperature θ_∞ inside of the free space generated by the crack opening, an consider the simple constitutive equations

$$q_C^{\pm}(\theta^{\pm}) = h_C(\theta^{\pm} - \theta_\infty) \quad \text{on } \boldsymbol{\varphi}_t^{\pm}(\Gamma) \tag{121}$$

as already considered for the exterior surfaces as defined in (107). Here, $\theta^{\pm}$ are the temperatures at the deformed crack faces $\gamma^{\pm}$ and h_C the *convective heat exchange parameter*. Hence, the total influx of heat through the crack faces is

$$Q^c := -\int_\Gamma (q^+ + q^-)\, dA = -\int_\Gamma 2h_C(\theta_m - \theta_\infty)\, dA \tag{122}$$

in terms of the *mean temperature* $\theta_m := (\theta^+ + \theta^-)/2$ defined on the sharp crack surface Γ. A transition of this sharp crack setting to the regularized phase field formulation is achieved by the transition of the crack surface element $dA \to \gamma_l(d; \nabla d)dV$ towards the volume element, governed by the crack surface density function $\gamma_l(d; \nabla d)$ defined in (9), yielding the approximation

$$Q^c \approx Q_l^c := -\int_{\mathcal{B}_0} 2h_C(\theta - \theta_\infty)\gamma_l(d; \nabla d)\, dV. \tag{123}$$

As a consequence of the spatial regularization, a convective heat exchange at crack faces can be described by an *additional heat source per unit volume*

$$r^c \approx -2h_C(\theta - \theta_\infty)\gamma_l = -2h_C(\theta - \theta_\infty)\frac{1}{2l}\big[d^2 + l^2|\nabla d|^2\big]. \tag{124}$$

Assuming both terms in the bracket of the same order, which is true for a damage profile of the form $d(x) = \exp[-|x|/l]$ in terms of a scalar coordinate x perpendicular to the crack, we may approximate (124) by the ansatz

$$\boxed{r^c \approx -2\frac{h_C}{l}(\theta - \theta_\infty)d^2} \tag{125}$$

Note that the function $g^c(d) = d^2$ models in the range $d \in [0, 1]$ a quadratic increase of the action of a convective heat exchange on the crack.

6. Time–space discretization of the bulk response

This section shortly comments on the space–time-discretization of the thermo-mechanical bulk response. This covers, together with the discretization of the crack phase field discussed in Section 2, the numerical model of thermo-elasticity at fracture.

6.1. Time-discrete field variables in incremental setting

Consider a finite time increment $[t_n, t_{n+1}]$, where $\tau_{n+1} := t_{n+1} - t_n > 0$ denotes the step length. All fields at time t_n are assumed to be *known*. The goal then is to determine the fields at time t_{n+1}. In order to keep the notation compact, subsequently all variables without subscript are evaluated at time t_{n+1}. An algorithm for the update of the temperature field θ in the increment $[t_n, t_{n+1}]$ can be based on the time-discrete form of the evolution equation (103), i.e.

$$\rho_0 c\dot{\theta}^\tau = -\mathrm{Div}[\mathbb{Q}^\alpha] + \rho_0 s^\alpha \quad \text{with } s^\alpha := r^\alpha + \mathcal{L}^\alpha + \mathcal{D}^\alpha_{loc} \tag{126}$$

in terms of the algorithmic expressions

$$\dot{\theta}^\tau := \frac{1}{\tau}(\theta - \theta_n) \quad \text{and} \quad (\cdot)^\alpha := (1-\alpha)(\cdot)_n + \alpha(\cdot). \tag{127}$$

Here, $\alpha \in [0, 1]$ is an algorithmic parameter which gives for $\alpha = 1$ the backward Euler scheme and for $\alpha = 1/2$ the trapezoidal rule. Note carefully that these algorithmic expressions are functions of the deformation field $\boldsymbol{\varphi}$ and the temperature field θ at the discrete time t_{n+1}.

6.2. Weak form of the time-discrete equations

The updates of the deformation and temperature in a typical time increment are governed by the balance of momentum $(91)_2$ and the time-discrete heat conduction equation (126). Their weak forms are constructed by standard Galerkin procedures. Let $\boldsymbol{X} \mapsto \delta\boldsymbol{\varphi} \in \mathcal{W}^\varphi_0 := \{\delta\boldsymbol{\varphi} | \delta\boldsymbol{\varphi} = 0 \text{ on } \partial\mathcal{B}^\varphi_0\}$ be the test function for the deformation, then

$$G^\tau_\varphi(\boldsymbol{\varphi}, \theta, d; \delta\boldsymbol{\varphi}) = \int_{\mathcal{B}_0} \{\boldsymbol{P} : \delta\boldsymbol{F} - \rho_0 \boldsymbol{\gamma} \cdot \delta\boldsymbol{\varphi}\}\, dV - \int_{\partial\mathcal{B}^t_t} \bar{\boldsymbol{t}} \cdot \delta\boldsymbol{\varphi}\, da = 0 \tag{128}$$

is the weak form of the balance of momentum, when inertia effects are neglected. Furthermore, let $\boldsymbol{X} \mapsto \delta\theta \in \mathcal{W}^\theta_0 := \{\delta\theta | \delta\theta = 0 \text{ on } \partial\mathcal{B}^\theta_0\}$ be the test function for the temperature, then

$$G^\tau_\theta(\boldsymbol{\varphi}, \theta, d; \delta\theta) = \int_{\mathcal{B}_0} \{\mathbb{Q}^\alpha \cdot \delta\mathbb{F} + \rho_0(s^\alpha - c\dot{\theta}^\tau)\delta\theta\}\, dV - \int_{\partial\mathcal{B}^h_t} \bar{q}^\alpha \delta\theta\, da = 0 \tag{129}$$

is the weak form of the temperature evolution equation.

6.3. Space–time-discrete finite element formulation

Now consider a standard finite element discretization of the spatial domain $\mathcal{B}_0$ of the *reference configuration* and Neumann surfaces $\partial\mathcal{B}^t_t$ and $\partial\mathcal{B}^h_t$ of the *current configuration*. We write

$$\mathcal{B}_0 = \bigcup_{e=1}^{N_e} \mathcal{B}^e_0, \qquad \partial\mathcal{B}^t_t = \bigcup_{s^t=1}^{N^t_s} \partial\mathcal{B}^{t\,s^t}_t, \qquad \partial\mathcal{B}^q_t = \bigcup_{s^q=1}^{N^q_s} \partial\mathcal{B}^{q\,s^q}_t, \tag{130}$$

where N_e is the number of *bulk finite elements*, N^t_s and N^q_s the numbers of *surface finite elements* for the mechanical tractions and the heat flow, respectively. The discretization by *bulk elements* $\mathcal{B}^e_0 \subset \mathcal{B}_0$ in the reference configuration is based on the finite element shapes

$$\begin{aligned} \boldsymbol{\varphi}^h(\boldsymbol{X}) &= \boldsymbol{N}^e_\varphi(\boldsymbol{X})\boldsymbol{d}_\varphi \\ \theta^h(\boldsymbol{X}) &= \boldsymbol{N}^e_\theta(\boldsymbol{X})\boldsymbol{d}_\theta \end{aligned} \quad \text{and} \quad \begin{aligned} \nabla\boldsymbol{\varphi}^h(\boldsymbol{X}) &= \boldsymbol{B}^e_\varphi(\boldsymbol{X})\boldsymbol{d}_\varphi \\ \nabla\theta^h(\boldsymbol{X}) &= \boldsymbol{B}^e_\theta(\boldsymbol{X})\boldsymbol{d}_\theta \end{aligned} \tag{131}$$

in terms of the matrices $\boldsymbol{N}^e_\varphi$ and $\boldsymbol{N}^e_\theta$ of bulk shape functions and their derivatives $\boldsymbol{B}^e_\varphi$ and $\boldsymbol{B}^e_\theta$. Here, $\boldsymbol{d}_\varphi$ and $\boldsymbol{d}_\theta$ are the space–time-discrete values of the deformation and the temperature at typical nodal points of the finite element mesh. The discretization of the Neumann surfaces by *surface elements* $\partial\mathcal{B}^{t\,s^t}_t \subset \partial\mathcal{B}^t_t$ and $\partial\mathcal{B}^{q\,s^q}_t \subset \partial\mathcal{B}^q_t$ is based on the finite

element shapes

$$\begin{aligned} \boldsymbol{\varphi}^h(\boldsymbol{x}) &= \boldsymbol{N}^s_\varphi(\boldsymbol{x})\boldsymbol{d}_\varphi \\ \theta^h(\boldsymbol{x}) &= \boldsymbol{N}^s_\theta(\boldsymbol{x})\boldsymbol{d}_\theta \end{aligned} \tag{132}$$

in terms of the matrices $\boldsymbol{N}^s_\varphi$ and $\boldsymbol{N}^s_\theta$ of surface shape functions. Insertion of shapes (131) and (132) into the time-discrete weak forms (128)–(129) and applying standard arguments give the coupled algebraic system

$$\begin{aligned} \boldsymbol{R}_{\boldsymbol{\varphi}}(\boldsymbol{d}_\varphi, \boldsymbol{d}_\theta; \boldsymbol{d}_d) &= \mathop{\mathsf{A}}_{e=1}^{N_e} \int_{\mathcal{B}^e_0} \{\boldsymbol{B}^{eT}_\varphi \boldsymbol{P} - \boldsymbol{N}^{eT}_\varphi \rho_0 \boldsymbol{\gamma}\}\, dV - \mathop{\mathsf{A}}_{s^t=1}^{N^t_s} \int_{\partial\mathcal{B}^{t\,s^t}_t} \boldsymbol{N}^{sT}_\varphi \bar{\boldsymbol{t}}\, da = \boldsymbol{0}, \\ \boldsymbol{R}_\theta(\boldsymbol{d}_{\boldsymbol{\varphi}}, \boldsymbol{d}_\theta; \boldsymbol{d}_d) &= \mathop{\mathsf{A}}_{e=1}^{N_e} \int_{\mathcal{B}^e_0} \{\boldsymbol{B}^{eT}_\theta \mathbb{Q}^\alpha + \boldsymbol{N}^{eT}_\theta \rho_0 (s^\alpha - c\dot{\theta}^\tau)\}\, dV - \mathop{\mathsf{A}}_{s^q=1}^{N^q_s} \int_{\partial\mathcal{B}^{q\,s^q}_t} \boldsymbol{N}^{sT}_\theta \bar{q}^\alpha\, da = \boldsymbol{0}. \end{aligned} \tag{133}$$

This is a coupled system for the determination of the nodal deformation and temperature $\boldsymbol{d}_\varphi$ and $\boldsymbol{d}_\theta$ at the current time t_{n+1} for given $\boldsymbol{d}_d$. Note that the nodal values $\boldsymbol{d}_d$ of the fracture phase field are updated by (41) within the one-pass operator split or a Gauss–Seidel scheme outlined in Box I.

6.4. Solution of the coupled algebraic finite element system

The algebraic system (133) can be solved at given $\boldsymbol{d}_d$ by standard methods for the solution of nonlinear equations. Introducing the compact notation for the global degrees and the residual of the finite element mesh

$$\boldsymbol{R} := [\boldsymbol{R}_\varphi\ \boldsymbol{R}_\theta]^T \quad \text{and} \quad \boldsymbol{d} := [\boldsymbol{d}_\varphi\ \boldsymbol{d}_\theta]^T, \tag{134}$$

we write the algebraic problem (133) as

$$\boldsymbol{R}(\boldsymbol{d}; \boldsymbol{d}_d) = 0. \tag{135}$$

A canonical solver is the Newton–Raphson iterations based on the updates

$$\boldsymbol{d} \Leftarrow \boldsymbol{d} - [D\boldsymbol{R}(\boldsymbol{d}; \boldsymbol{d}_d)]^{-1} \boldsymbol{R}(\boldsymbol{d}; \boldsymbol{d}_d) \tag{136}$$

until convergence is achieved in the sense $\|\boldsymbol{R}\| < tol$. It is based on a full linearization of the nonlinear algebraic system based on the monolithic tangent $D\boldsymbol{R}$. This provides the incremental solution of the thermo-elastic bulk response associated with step 3 in Box I that follows the update for the fracture phase field in step 2. The subsequent numerical investigations use *one-pass operator splits* in line with treatments in Miehe [42], Miehe et al. [2]. Such an algorithmic setting is extremely robust and considered to be the most simple scheme for the treatment of diffusive fracture in thermo-elastic solids.

7. Numerical model investigations

This section demonstrates the performance of the continuum phase field model for fracture in thermo-elastic solids by means of some representative numerical examples. The model simulations are conceptual in nature and designed such that the modeling capacity of fundamental coupling phenomena of fracturing thermo-elastic solids at finite strains are highlighted. In particular, the subsequent simulations demonstrate

- the performance of phase field fracture with the *stress criterion* $\tilde{D}$ defined in (61),
- the temperature increase at crack faces due to the *dissipative heating* $\mathcal{D}_{loc}$ in (103),
- the generation of a *convective heat exchange* via the source r^c defined in (125),
- the *cracking* due to inhomogeneous stress fields *induced by thermal expansion* (110).

The material parameters used in the subsequent simulations are related to rubber-like polymers which show thermo-elastic behavior at finite strains, see for example Miehe [42]. We focus on a rate-independent setting of crack propagation for $\eta = 0$. A basic set of parameters is given in Table 1. In what follows, some of these values are modified in order to emphasize particular effects. This is commented on in the description of the examples.

Table 1
Material parameters.

No.	Parameter	Name	Eq.	Value	Unit
1	μ	Shear modulus	(109)	1.0	MPa
2	ν	Poisson's ratio	(109)	0.45	–
3	α	Linear thermal expansion	(110)	1×10^{-3}	K^{-1}
4	k^s	Thermal conductivity	(113)	0.1	N/K s
5	$\rho_o c$	Heat capacity	(111)	10	MPa/K
6	h_C	Surface convection	(107)	5	N/(s mm K)
7	θ_∞	Ambient temperature	(107)	273	K
8	σ_c	Critical stress	(61)	2.0	MPa
9	ζ	Driving force slope	(61)	1	–
10	l/h	Length scale/mesh ratio	(32)	≈ 2	–

7.1. Fracture and dissipative heat generation in bending test

This example demonstrates the performance of the phase field model for fracture at large strains and the thermo-mechanical coupling effect, i.e. temperature increase due to the dissipative crack propagation. We perform a bending test of a simply supported notched beam under plane strain conditions, shown in Fig. 10. The dimensions are 40 mm in width and 10 mm in height. The supports are located 4 mm inwards from the outer edge, the load is applied in the middle of the upper edge by prescribed deformation. There is a tiny initial notch of length 0.125 mm in the middle of the lower edge. The mesh is refined in the areas where the crack is expected to propagate. Exploiting symmetry, a discretization of half the specimen with 1550 elements and an effective element size in the refined region of $h = 0.0625$ mm is used. The computation is performed in a displacement-driven context. As expected, the material in the top region of the beam is compressed while the material at the bottom is stretched. Fig. 10(b) shows the nominal stress distribution P_{11} in axial direction. The stress-based crack driving state function $\tilde{D}$ defined in (61) starts to evolve once the threshold σ_c is reached. Then the crack phase field evolves and the crack grows from the initial notch towards the top region of the beam. At two stages during crack propagation the phase field is depicted in Fig. 10(c). The blue color corresponds to virgin, undamaged material, whereas fully damaged continuum (or free space continuum) is represented by red color. The dissipation $\mathcal{D}_{loc}$ due to phase field evolution defined in (99) enters the temperature evolution equation (103) and causes an increase of temperature in regions close to the crack faces. This is shown in Fig. 10(d). This temperature increase is small, with a maximum value of 0.5 K. Here, the level set function $\Gamma_c = \{\boldsymbol{X} \mid d = c\}$ introduced in Fig. 1 is used to visualize the crack opening and the temperature state.

Fig. 11 investigates effects due to the length-scale l and the driving force slope parameter ζ introduced in (61). For a fixed ratio of length-scale to element size $l_1/h = 2$, the influence of ζ is analyzed. Load–deflection curves for different values $\zeta = \{40, 50, 60, 100\}$ are depicted in Fig. 11(a). Note the convergence towards the ideal local stress limit σ_c for increasing ζ, the curves $\zeta = \{60, 100\}$ almost coincide. This is a structural counterpart to the homogeneous problem investigated in Fig. 4(c). The influence of the length scale l is analyzed at fixed $\zeta = 60$ for three simulations with $l_1/h = 2$, and $l_2/h = 4$ and $l_3/h = 6$. As shown in Fig. 11(b), the overall structural response is not very sensitive to the length scale l. The curves nearly coincide.

7.2. Fracture of inhomogeneous strip under tension

This example shows a boundary value problem a curvilinear crack develops. A rectangular strip of 60 mm width and 30 mm height with two eccentric holes of diameter 10 mm is analyzed for tensile loading. The geometry is depicted in Fig. 12. The elastic constants in Table 1 are modified for this example to $\mu = 0.19$ and $\nu = 0.45$. No initial crack is introduced, the crack phase field d starts to evolve where stress concentrations occur. When the specimen is loaded, an inhomogeneous stress distribution in the strip develops with maximal values at top and bottom positions of the holes. Once these values exceed the threshold σ_c, a crack initiates and grows fast through the narrow strip towards the edge. The growth takes place in the direction of maximal stress. After the rupture of the narrow strip, stresses develop towards a maximum at the opposite side of the holes. There a new crack initiates, growing through the specimen in the direction of maximal principal tensile stress. Fig. 13 shows the stress P_{11} on the deformed configuration and shows

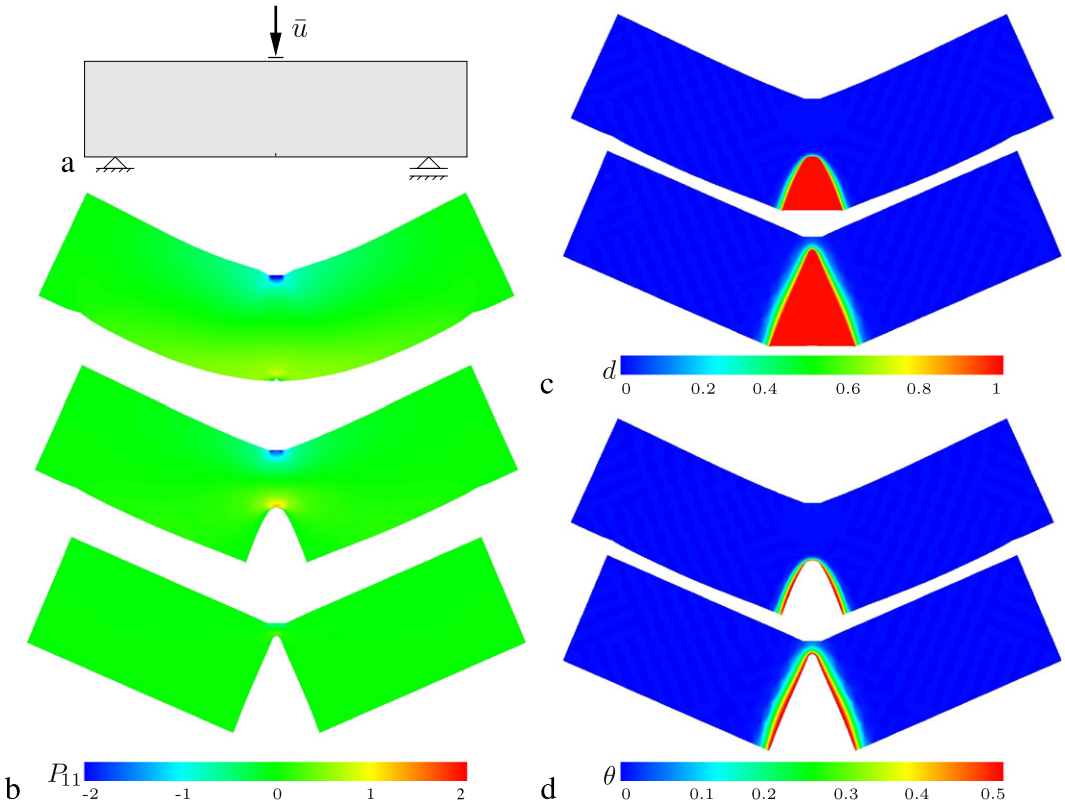

Fig. 10. Three point bending test. (a) Geometry, (b) Stress contour, (c) phase field contour and (d) temperature increase due to dissipation for several displacements. (For interpretation of the references to color in this figure legend, the reader is referred to the web version of this article.)

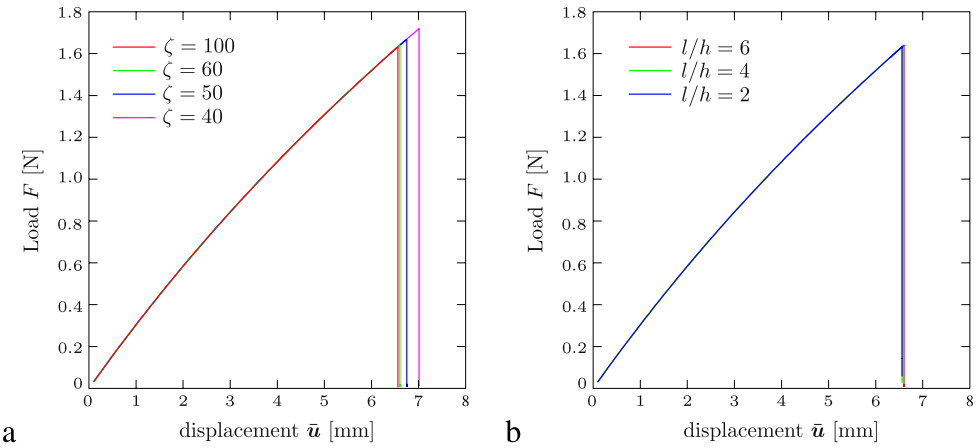

Fig. 11. Three point bending test. (a) Sensitivity of structural response on driving force slope factor ζ introduced in (61). Curves for $\zeta = 60$ and $\zeta = 100$ almost coincide. (b) Influence of length scale l at fixed $\zeta = 60$. Curves for $l/h = \{2, 4, 6\}$ almost coincide.

different stages of failure of the deformation controlled problem. As shown in the last plot, the specimen breaks into three parts.

7.3. Heat flux response at evolving cracks in notched tension test

This example demonstrates alternative constraints for the heat flux at evolving crack faces at large strains. A rectangular specimen of width 40 mm and height 10 mm with a horizontal centered notch of 10 mm width is loaded

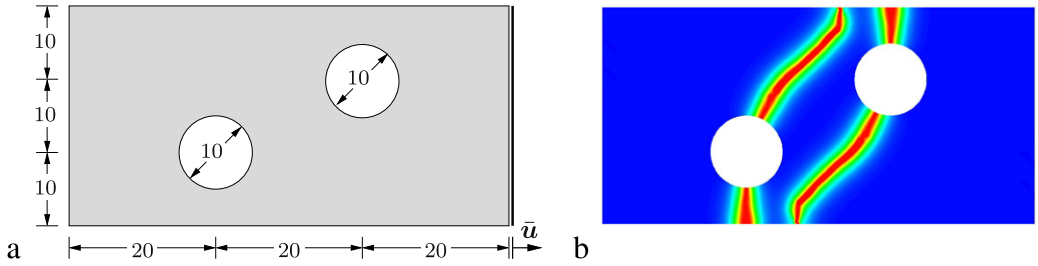

Fig. 12. Inhomogeneous strip under tension. (a) Geometry with all dimensions in (mm), (b) crack phase field d of final state on reference configuration.

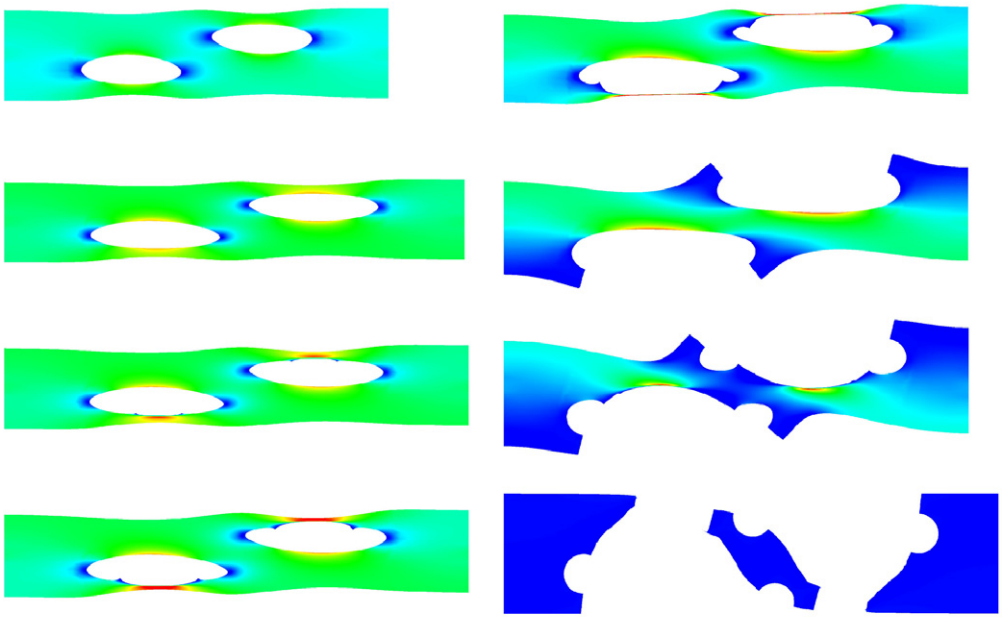

Fig. 13. Inhomogeneous strip under tension. Stress distribution P_{11} for different stages of the deformation controlled loading process. Depicted are states at the onset of crack evolution and crack growth towards a fully fractured state.

by a controlled displacement of its top. In addition, a *steady-state* heat flux from the top to the bottom region is enforced by prescribed temperature at the surfaces. The geometry including the mechanical and thermal boundary conditions are depicted in Fig. 14(a). The mesh is refined in areas where the crack is expected to propagate, i.e. in a centered horizontal strip of the specimen. Exploiting symmetry, a discretization of the half specimen with 5300 elements with an effective element size of $h \approx 0.05$ mm in the refined zone is applied. For this simulation, we modify some parameters of Table 1 towards $\mu = 0.19, \sigma_c = 50, c = 0, k^s = 10$ and $\alpha = 0$, in order to focus on basic effects associated with the heat flux. The computation is performed in a monotonic displacement-driven context. The temperature field is increased at the top by $\theta^+ = 10$ K and decreased at the bottom by $\theta^- = -10$ K in relation to the ambient temperature θ_∞.

Three simulations are performed which show alternative treatments of heat flux $\mathbb{Q}^c$ across the crack modeled by the phase transition of the dissipation function defined in (120). In the first case in Fig. 14(a), *no degradation of the heat flux* is considered, i.e. $k^c = k^s$ in (113). The temperature on the deformed specimen is shown in Fig. 15(a) for two crack states, including the final separation of the specimen into two parts. An intermediate state is depicted in Fig. 14(b), where the phase field d and the temperature changes θ are plotted, respectively. The plot of the phase field shows in blue color undamaged material and in red color the fully broken continuum, where a crack at large strains has developed. For non-degraded conductivity, the generated *free space part* still conducts heat as if it was

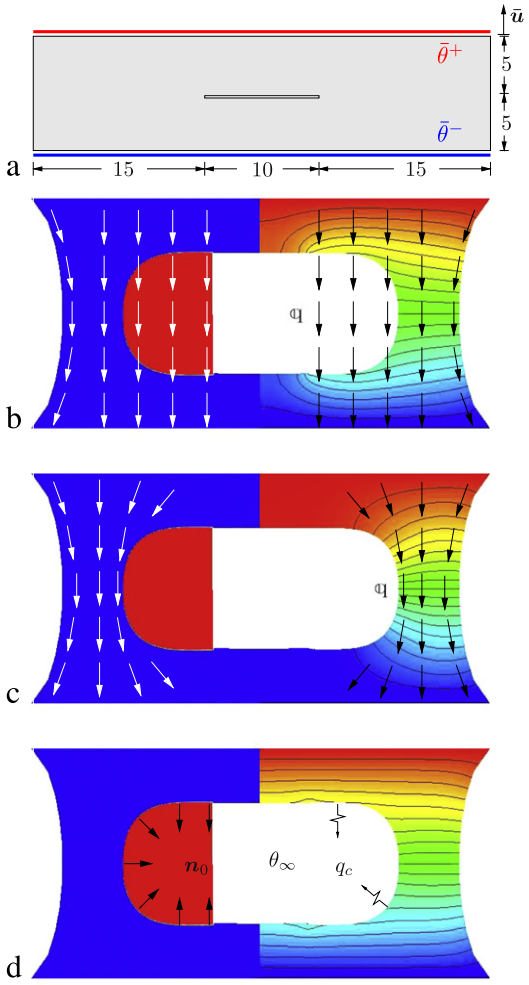

Fig. 14. Notched tension test with prescribed temperature at boundaries. (a) Geometry in (mm), discretization with quadrilateral elements, and boundary conditions. In the subsequent plots: on left the phase field d and on right the temperature θ. (b) Heat flux $\mathbb{q}$, indicated by arrows, with unphysical conduction $k^c = k^s$ through crack. (c) Heat flux $\mathbb{q}$ for impermeable crack $k^c = 0$ that surrounds the crack tip. (d) Convective heat exchange q_C with ambient temperature θ_∞, modeled by the heat source r^c defined in (125). (For interpretation of the references to color in this figure legend, the reader is referred to the web version of this article.)

undamaged. The arrows in the picture symbolize the spatial heat flux $\mathbb{q}^c$ and visualize the conduction through the free space. Obviously, this result is unphysical.

The second case study considers a *fully degrading bulk conductivity*, i.e. $k^c = 0$ in (113). The temperature field during crack growth is depicted for two deformation states in Fig. 15(b). For an intermediate state, Fig. 14(c) shows the contours of the fracture phase field d and the temperature changes θ. Again, red color represents fully broken continuum, i.e. the generated free space. Due to the vanishing conductivity in the free space, the spatial heat flux $\mathbb{q}^c$ becomes deformation-dependent and the heat flow surrounds the crack. This is indicated by the arrows. Because the conductivity of the free space is assumed to be zero, a thermally impermeable solution is obtained. Consequently, the temperature contour lines are perpendicular to the newly created crack surfaces. Fig. 15(b) shows that the continuing crack evolution finally divides the specimen into two parts with homogeneous distributions of the temperature. The temperature changes of these two parts are prescribed by the corresponding boundary conditions at the top and bottom surfaces, respectively.

The third simulation represents a realistic scenario. Besides of the *fully degrading bulk conductivity*, it additionally takes into account a *convective heat exchange on generated crack surfaces*, i.e. a convection to a surrounding medium in the free space. This is realized in the context of the phase field description of fracture by the additional heat source

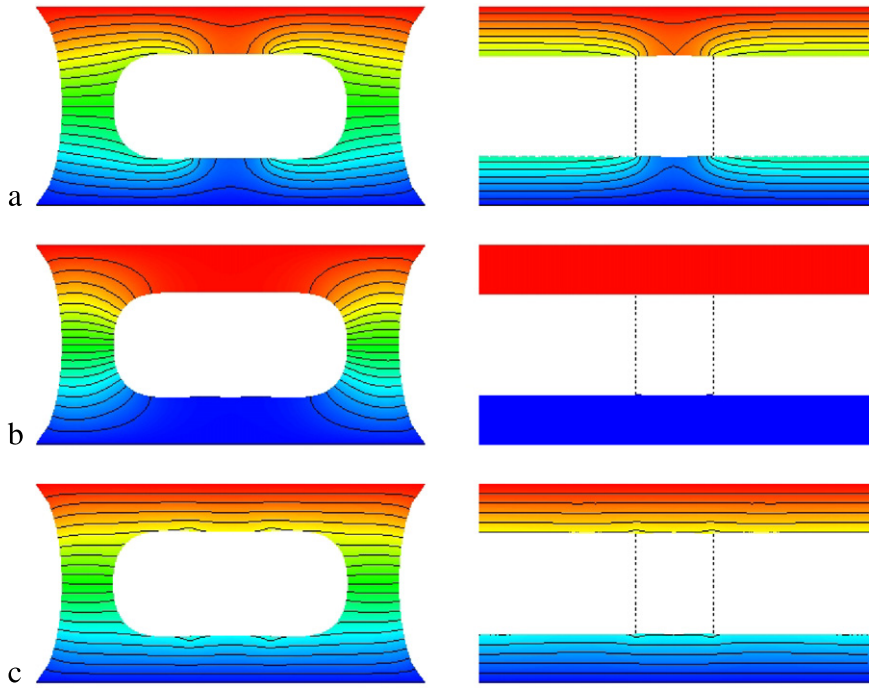

Fig. 15. Notched tension test with prescribed temperature at boundaries. Temperature field on deformed configuration at an initial phase of the crack progress and for fully fractured specimen. (a) Non-degraded conductivity $k^c = k^s$ yielding unphysical conduction through crack. (b) Fully degraded conductivity $k^c = 0$ for impermeable crack and two thermally decoupled fractured pieces. (c) Convective heat exchange on notch and created crack surface to surrounding medium. The dotted lines indicate the position of the initial notch.

r^c defined in (125). In addition to the prescribed temperature changes $\theta^+ = 10$ K and $\theta^- = -10$ K at the top and bottom surfaces, convection is introduced according to (121) in the free space of the initial crack and the additional free space generated by the crack propagation. The exchange coefficient is set to $h_C = 1$ N/(s mm K). Fig. 15(c) depicts the temperature changes at two deformation states. As shown in the picture, the temperature on the initial notch surface and the newly created crack surface are equal. Especially at the final state in Fig. 15(c), when the specimen is split into two parts, the influence of surface convection on the temperature is instructive. Here, in order to the separate the initial horizontal notch from the newly generated crack surface we introduce dotted lines. In the zone where convection influences the temperature on the body, the temperature field shows a uniform distribution, in the zone of the initial notch as well as on the crack faces.

7.4. Thermal induced crack propagation in a circular plate

The aim of this example is to model crack propagation in solids induced by inhomogeneous stress fields triggered by thermal expansion. To this end, a circular plate with radius $r = 1$ mm and with a tiny initial notch of $0.025\,r$ is subjected to thermal loading. Exploiting symmetry, half the specimen is discretized with 4200 elements, the mesh is refined to $h \approx 0.00625$ mm in the zone of expected crack propagation. A convective heat exchange q_C defined in (107) is applied on the full surface of the specimen, and modeled on crack faces by the heat source r^c defined in (125). The initial body temperature $\theta(t = 0) = 300$ °C whereas the ambient temperature is set to $\theta_\infty = 0$ °C and the convection coefficient is set $h = 0.1$ N/(s mm K). By these boundary conditions, a transient temperature field in the bulk of the specimen is obtained. This process causes a thin layer with a high temperature gradient and a core with almost no temperature change. The thermally induced contraction of the boundary layer induces tension tangentially to the surface of the specimen. At the tip of a tiny notch the stresses concentrate and exceed the critical value σ_c in the crack driving state function $\tilde{D}$ defined in (61), and thus fracture is induced. First, the crack speed is very high so the crack evolves instantaneously. Then, the crack speed slows down and at some state the crack stops growing. While the crack opens, the contraction of the boundary layer is bending the body open. The crack surfaces

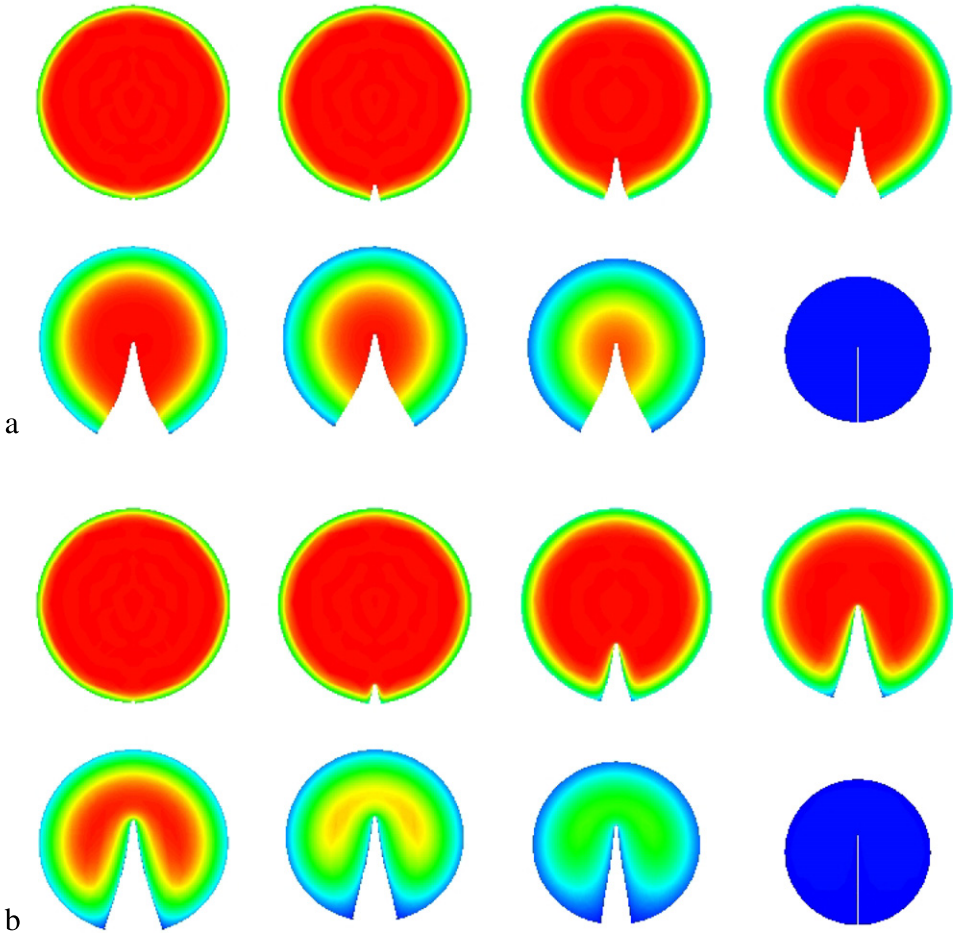

Fig. 16. Circular body with initial notch and prescribed temperature decrease at boundary. Transient temperature field due to surface convection to medium with linearly decreasing ambient temperature. Due to the inhomogeneous temperature gradient, the boundary contracts, leading to tensile stresses which create cracks. Temperature distribution (a) without and (b) with convection on crack faces, modeled by the heat source r^c in (125) at the times $t = \{4.85, 6.5, 15.3, 25.3, 50, 90, 140, 1000\}$ s.

obtain a convex curved shape. The surface convection is cooling down the specimen, until after a long period of time, the full body has adapted the ambient temperature and recovered the circular form. Fig. 16(a) shows the temperature change with the thin layer of high gradients when *only the degrading bulk convectivity is considered* at the times $t = \{4.85, 6.5, 15.3, 25.3, 50, 90, 140, 1000\}$ s.

The test is repeated by considering not only the convection on the outer surface, but also a *convective heat exchange at the generated crack surfaces* modeled by the additional heat source r^c defined in (125). The resulting temperature changes are depicted in Fig. 16(b). As long as the crack propagates with a high speed the results resemble the ones of the previous example. When the crack speed slows down and crack arrests, the surface convection on the crack surface becomes visible. The surface convection is cooling down the specimen, until after $\approx$1000 s, the full body has adapted the ambient temperature and recovered the circular form.

7.5. Thermal shock induced crack in a brittle solid

This example demonstrates the evolution of thermally induced complex crack patterns. An experimental study of Geyer and Nemat-Nasser [43] on thermally induced cracks in brittle solids is simulated. An analysis of this problem was recently outlined in Sicsic et al. [44] and Bourdin et al. [45]. In the experiment, a glass slab with uniform temperature is brought into contact with dry ice. Because of the cooling of the contacting edge, a thermal boundary layer develops in the solid within a transient process, yielding thermally induced cracks. In order to simulate

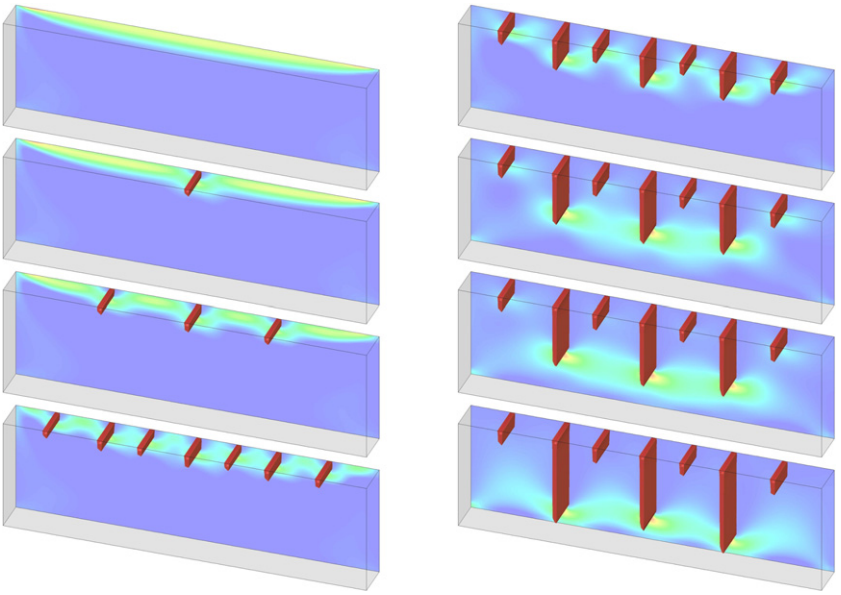

Fig. 17. Thin glass plate, clamped at the bottom. Prescribed temperature drop of -100 K on the upper surface leads to contraction and to natural tensile transversal stress with maximum in the middle of the upper edge. Cracks open up, partitioning the upper surface in regular segments. Stress plots and evolving cracks at $t = \{6.1, 6.78, 7.36, 9.33, 24.2, 60, 84, 1550\}$ s.

this effect, a rectangular plate of width 100 mm and height 30 mm is discretized. The bottom surface is fixed in all directions and the temperature is held constant at $\theta = 22$ °C. The thermal loading through contact is modeled by a Dirichlet-type control of the temperature field at the upper surface. In a period of 10 s, the temperature is linearly decreased from $\bar{\theta} = 22$ °C to a minimum of $\bar{\theta} = -78$ °C which is then held constant. The shock-like thermal stimulation leads to contraction and a natural tensile transversal stress in a thin layer. Through the natural stress state, a maximum in the middle of the upper surface evolves, leading to a first crack there. In Fig. 17 the stress P_{11} and the evolving cracks are shown at the times $t = \{6.1, 6.78, 7.36, 9.33, 24.2, 60, 84, 1550\}$ s. With ongoing cooling, the stress on the upper surface again becomes maximum in the middle of the partitions, producing secondary cracks. This process repeats once more. Because of the ongoing conduction process crack grow perpendicular to the cooled edge, however, alternate cracks stop at critical instable point, while the remaining ones continue to grow. When a homogeneous temperature gradient between upper and lower surface is obtained, all cracks end. The results are in good qualitative agreement with the experiments reported in Geyer and Nemat-Nasser [43].

7.6. Shattering of a solid brick under a thermal shock

A brick with dimensions $100 \times 100 \times 30$ mm is discretized with 153,000 linear brick elements. The top surface is fixed and all other surfaces are unconstrained. Resembling a natural state, the critical stress parameter σ_c is assumed to be in-homogeneously distributed. It is 50 kN/mm^2 in some randomly located flaws and 52 kN/mm^2 otherwise. The cooling process is induced by a prescribed temperature at the bottom surface.

The surface temperature $\vartheta := \theta - \theta_0$ decreases linearly from zero to -100 °C in 10 s and is then held constant. On the back and bottom sides of the brick, the temperature is displayed. The decreasing temperature at the bottom surface leads to contraction and a transversely tensile stress in a thin layer. Once the resulting stress exceeds the critical value, cracks initiate. When cooling continues, more cracks initiate and the existing ones grow. The depth of the damaged zone is growing and alternate cracks grow deeper, while others stop growing. Finally the cracks form a honeycomb structure. Fig. 18 shows the crack surfaces and the temperature distribution at the times $t = \{6, 14, 20.5, 28.5, 45, 65\}$ s. The example demonstrates the ability of the proposed phase field formulation of fracture to predict complex crack patterns including crack initiation, curved cracking and crack arrest.

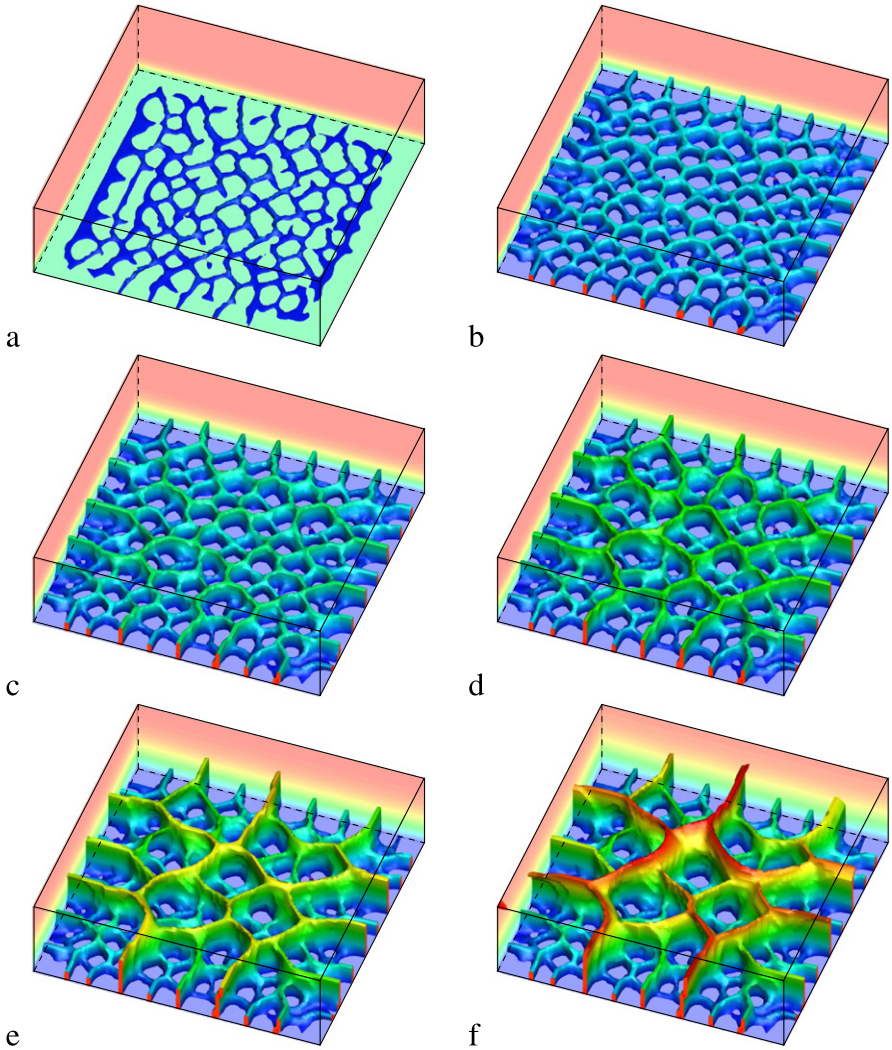

Fig. 18. Thermally induced crack in a soil block. (a) Thermal stimulation in a thin layer with initialization of first cracks. (b) The temperature conduction is continuing, thus more cracks initiate and the existing ones grow. (c–e) The depth of the cooled layer is growing, thus the cracks grow in depth. (f) Thermal conduction process and crack growth are slowing down until a steady state is obtained.

7.7. Crack evolution in a two-phase composite material

This example treats the crack evolution in different types of two-phase materials. Numerous ceramic materials of commercial comprise a crystalline phase embedded in a glass matrix. The strength controlling factors are the expansion coefficients of the two phases, the volume fraction, particle size and the elastic properties. Davidge and Green [46] studied the effect of these mechanical properties on stresses around particles. Different types of glasses containing 10% thoria spheres were prepared and tested. Of these, we investigate two different composites with $\mu_M = 29,166$ MPa, $\nu_M = 0.2$ and $\mu_S = 97,847$ MPa, $\nu_S = 0.275$ for the matrix and the spheres, respectively. The expansion coefficient of the spheres is $\alpha_S = 8.7 \times 10^{-6}$. In *composite* 1 the matrix expansion coefficient is $\alpha > \alpha_{M1} = 6.8 \times 10^{-6}$, whereas in *composite* 2 the matrix expands more than the spheres $\alpha < \alpha_{M2} = 10.5 \times 10^{-6}$. Sphere–matrix interaction inducing fracture occurs either after fabrication due to differences in thermal expansion or due to the influence of an externally applied load. Stresses around the spheres originate from production process of vacuum hot-pressing at around 700 °C followed by a cooling down. *Composite* 1 with particle contracting more than the matrix develops positive stresses in the spheres, see Fig. 19(a), whereas *composite* 2 shows maximum positive stresses around the particles, see Fig. 19(b). Further cooling induces spontaneous microcracks at the interfaces. At a

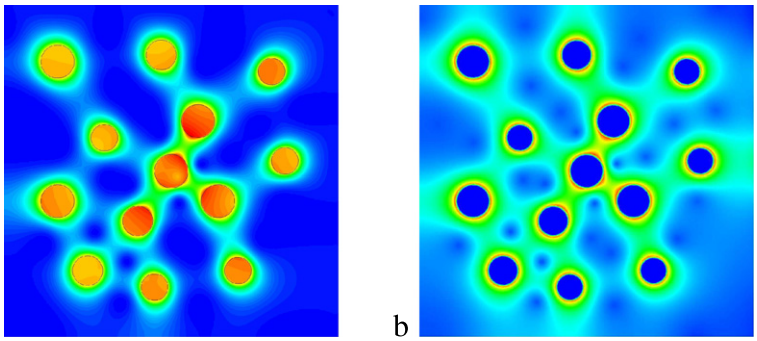

Fig. 19. Cooling from manufacturing temperature of ≈700 °C to room temperature induces stresses around the spheres due to differences in the expansion coefficients of the glass and the spheres. (a) Particle contracting more than the matrix develops positive stresses inside the spheres, whereas (b) a stronger contracting matrix shows maximum positive stresses around the particles.

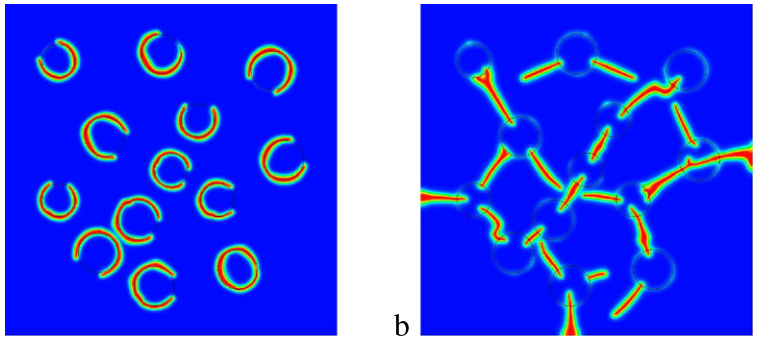

Fig. 20. Cooling from manufacturing temperature of ≈700 °C to very low temperature values leads to a spontaneous cracking of the matrix in radial direction of the spherical inclusions or to a fall out of the spheres.

very low temperature the stresses around the spheres exceed the critical stresses σ_c initiating cracks. The nature of cracking depends on the type of composite. In *composite* 1, cracks occur on the phase boundaries in a circumferential way, separating the spheres from the matrix, see Fig. 20(a). In the opposite case *composite* 2, cracks initiate on the boundaries and grow radial between the spheres into the matrix breaking the body into fragments, see Fig. 20(b). These failure mechanisms occur by thermal contraction only.

The influence of sphere matrix interaction on the fracture of an *externally loaded* plate at room temperature is also studied. Therefore the cooling from production process to room temperature is simulated first, followed by a simple tensile loading in vertical direction. The internal residual stress state occurring from particle and matrix contraction is already shown in Fig. 19. The stresses which arise from the deformation controlled loading are superimposed to the internal residual stresses. Since the inclusions are stiffer than the matrix, the inclusions reach the higher stresses. *Composite* 1 shows high stresses inside the spheres and on the interfaces. Tangential cracks develop at all sphere boundaries in the brittle matrix. Cracks in higher stressed regions in the matrix propagate around the spheres and approach each other. Finally the plate is separated into two pieces. The internal residual stresses in the spheres are almost relieved, see Fig. 21a. *Composite* 2 shows tensile tangential stresses in the matrix–sphere interface. A single crack is growing from the boundary inside the matrix. It is directed towards the spheres and either grows along the interfaces or pass through the spheres. The Internal residual stresses around the uncracked spheres remain in the fragments (see Fig. 21b).

8. Conclusion

We outlined a generalization of recently developed continuum phase field models for brittle fracture towards fully coupled thermo-mechanical and multi-physics problems at large strains. A key ingredient of this treatment was a rigorous geometric approach to the *diffusive* crack modeling based on the introduction of a *balance of regularized crack surface*, governed by a crack phase field. The regularized crack surface functional was based on a crack surface density function, that approximates the macroscopic crack surface in the bulk material per unit of the reference volume.

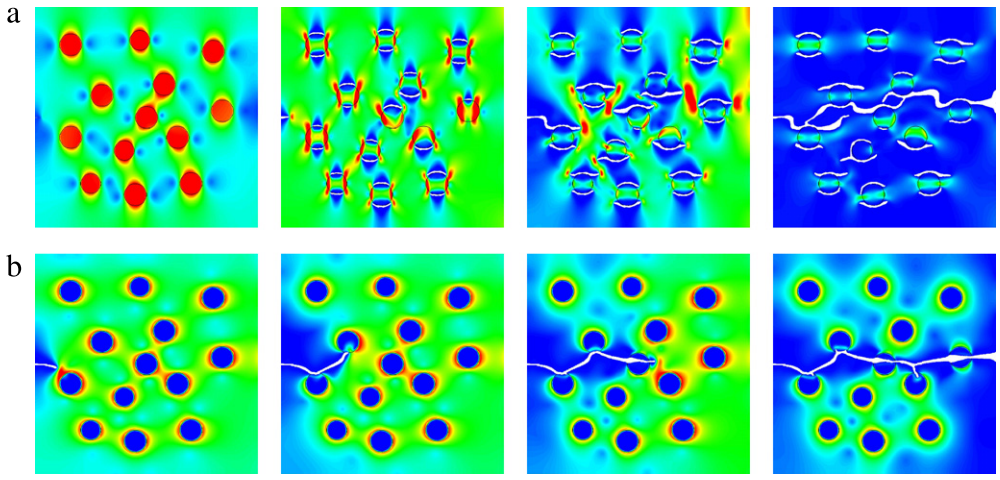

Fig. 21. Plate under tensile loading. (a) *Composite* 1 with high internal residual stresses inside the spheres. Cracks in the brittle matrix propagate around the spheres inside the matrix and separate the plate. Internal residual stresses are almost relieved. (b) *Composite* 2 with tensile tangential stresses in the matrix–sphere interface. The crack is directed towards the spheres and eventually cracking of the spheres is observed. Internal residual stresses remain in the fragments.

The approach overcomes difficulties associated with the computational realization of *sharp* crack discontinuities, in particular when it comes to complex crack topologies. The formulation proposed is essentially a gradient damage theory, however, equipped with critical ingredients rooted in fracture mechanics. A *modular concept* for the linking of the diffusive crack modeling with *complex multi-field material response* of the bulk material was outlined, where we focused on the model problem of finite thermo-elasticity. This included a *generalization of crack driving forces* from the energetic definitions towards *stress-based criteria*, the constitutive modeling of *heat conduction* across cracks, the generation of *convective heat exchanges* based on additional constitutive functions defined at the crack faces. This was achieved by approximating surface load integrals of the sharp crack approach by distinct volume integrals. The performance of the phase field formulation of fracture was demonstrated by means of conceptual numerical examples. Future work will extend the formulation to ductile fracture in thermo-plastic solids.

Acknowledgment

Support for this research was provided by the German Research Foundation (DFG) within the Cluster of Excellence Exc 310 *Simulation Technology* at the University of Stuttgart.

References

[1] C. Miehe, F. Welschinger, M. Hofacker, Thermodynamically consistent phase-field models of fracture: Variational principles and multi-field FE implementations, Internat. J. Numer. Methods Engrg. 83 (2010) 1273–1311.
[2] C. Miehe, M. Hofacker, F. Welschinger, A phase field model for rate-independent crack propagation: Robust algorithmic implementation based on operator splits, Comput. Methods Appl. Mech. Engrg. 199 (2010) 2765–2778.
[3] M.J. Borden, C.V. Verhoosel, M.A. Scott, T.J.R. Hughes, C.M. Landis, A phase-field description of dynamic brittle fracture, Comput. Methods Appl. Mech. Engrg. 217–220 (2012) 77–95.
[4] M.J. Borden, T.J.R. Hughes, C.M. Landis, C.V. Verhoosel, A higher-order phase-field model for brittle fracture: Formulation and analysis within the isogeometric analysis framework, Comput. Methods Appl. Mech. Engrg. 273 (2014) 100–118.
[5] C.V. Verhoosel, R. de Borst, A phase-field model for cohesive fracture, Internat. J. Numer. Methods Engrg. 96 (2013) 43–62.
[6] L. Ambrosio, V.M. Tortorelli, Approximation of functionals depending on jumps by elliptic functionals via Γ-convergence, Comm. Pure Appl. Math. 43 (1990) 999–1036.
[7] L. Ambrosio, V.M. Tortorelli, On the approximation of free discontinuity problems, Boll. Unione Mat. Ital. 6-B (1992) 105–123.
[8] G. Dal Maso, An Introduction to Γ-Convergence, Birkhäuser, 1993.
[9] D.P. Braides, Γ-Convergence for Beginners, Oxford University Press, 2002.
[10] D.P. Braides, Approximation of Free Discontinuity Problems, Springer Verlag, Berlin, 1998.
[11] V. Hakim, A. Karma, Laws of crack motion and phase-field models of fracture, J. Mech. Phys. Solids 57 (2009) 342–368.
[12] A. Karma, D.A. Kessler, H. Levine, Phase-field model of mode III dynamic fracture, Phys. Rev. Lett. 87 (2001) 045501.

[13] L.O. Eastgate, J.P. Sethna, M. Rauscher, T. Cretegny, Fracture in mode I using a conserved phase-field model, Phys. Rev. E 65 (2002) 036117.
[14] C. Kuhn, R. Müller, A continuum phase field model for fracture, Eng. Fract. Mech. 77 (2010) 3625–3634.
[15] G.A. Francfort, J.J. Marigo, Revisiting brittle fracture as an energy minimization problem, J. Mech. Phys. Solids 46 (1998) 1319–1342.
[16] B. Bourdin, G. Francfort, J.-J. Marigo, The Variational Approach to Fracture, Springer, 2008.
[17] G. Capriz, Continua with Microstructure, Springer, 1989.
[18] P.M. Mariano, Multifield theories in mechanics of solids, Adv. Appl. Mech. 38 (2001) 1–93.
[19] M. Frémond, Non-Smooth Thermomechanics, Springer, 2002.
[20] C. Miehe, A multi-field incremental variational framework for gradient-extended standard dissipative solids, J. Mech. Phys. Solids 59 (2011) 898–923.
[21] M. Frémond, B. Nedjar, Damage, gradient of damage, and principle of virtual power, Internat. J. Solids Structures 33 (1996) 1083–1103.
[22] R.H.J. Peerlings, R. de Borst, W.A.M. Brekelmans, J.H.P. de Vree, Gradient enhanced damage for quasi-brittle materials, Internat. J. Numer. Methods Engrg. 39 (1996) 3391–3403.
[23] C. Comi, Computational modelling of gradient-enhanced damage in quasi-brittle materials, Mech. Cohes.-Frict. Mater. 4 (1999) 17–36.
[24] C. Comi, U. Perego, Fracture energy based bi-dissipative damage model for concrete, Internat. J. Solids Structures 38 (2001) 6427–6454.
[25] K. Pham, H. Amor, J. Marigo, C. Maurini, Gradient damage models and their use to approximate brittle fracture, Int. J. Damage Mech. 20 (2011) 618–652.
[26] X.P. Xu, A. Needleman, Void nucleation by inclusion debonding in a crystal matrix, Modelling Simul. Mater. Sci. Eng. 1 (1993) 111–132.
[27] M. Ortiz, A. Pandolfi, Finite-deformation irreversible cohesive elements for three-dimensional crack-propagation analysis, Internat. J. Numer. Methods Engrg. 44 (1999) 1267–1282.
[28] C. Miehe, E. Gürses, A robust algorithm for configurational-force-driven brittle crack propagation with R-adaptive mesh alignment, Internat. J. Numer. Methods Engrg. 72 (2007) 127–155.
[29] E. Gürses, C. Miehe, A computational framework of three-dimensional configurational-force-driven brittle crack propagation, Comput. Methods Appl. Mech. Engrg. 198 (2009) 1413–1428.
[30] J.C. Simo, J. Oliver, F. Armero, An analysis of strong discontinuities induced by strain-softening in rate-independent inelastic solids, Comput. Mech. 12 (1993) 277–296.
[31] J. Oliver, Modelling strong discontinuities in solid mechanics via strain softening constitutive equations. Part 1: Fundamentals, Internat. J. Numer. Methods Engrg. 39 (1996) 3575–3600.
[32] J. Oliver, Modelling strong discontinuities in solid mechanics via strain softening constitutive equations. Part 2: Numerical simulation, Internat. J. Numer. Methods Engrg. 39 (1996) 3601–3623.
[33] C. Linder, F. Armero, Finite elements with embedded branching, Finite Elem. Anal. Des. 45 (2009) 280–293.
[34] N. Moës, J. Dolbow, T. Belytschko, A finite element method for crack growth without remeshing, Internat. J. Numer. Methods Engrg. 46 (1999) 131–150.
[35] G.N. Wells, L.J. Sluys, A new method for modelling cohesive cracks using finite elements, Internat. J. Numer. Methods Engrg. 50 (2001) 2667–2682.
[36] T.C. Gasser, G.A. Holzapfel, Modeling 3D crack propagation in unreinforced concrete using pufem, Comput. Methods Appl. Mech. Engrg. 194 (2005) 2859–2896.
[37] T. Belytschko, H. Chen, J. Xu, G. Zi, Dynamic crack propagation based on loss of hyperbolicity and a new discontinuous enrichment, Internat. J. Numer. Methods Engrg. 58 (2003) 1873–1905.
[38] J.-H. Song, T. Belytschko, Cracking node method for dynamic fracture with finite elements, Internat. J. Numer. Methods Engrg. 77 (2009) 360–385.
[39] M.H. Protter, H.F. Weinberger, Maximum Principles in Differential Equations, Springer-Verlag, 1984.
[40] A. Benallal, J. Marigo, Bifurcation and stability issues in gradient theories with softening, Modelling Simul. Mater. Sci. Eng. 15 (2007) S283.
[41] S. Lu, K. Pister, Decomposition of the deformation and representation of the free energy function for isotropic thermoelastic solids, Internat. J. Solids Structures 11 (1975) 927–934.
[42] C. Miehe, Entropic thermoelasticity at finite strains. Aspects of the formulation and numerical implementation, Comput. Methods Appl. Mech. Engrg. 120 (1995) 243–269.
[43] J. Geyer, F. Nemat-Nasser, Experimental investigation of thermally induced interacting cracks in brittle solids, Internat. J. Solids Structures 18 (1982) 349–356.
[44] P. Sicsic, J.J. Marigo, C. Maurini, Initiation of a periodic array of cracks in the thermal shock problem: A gradient damage modeling, J. Mech. Phys. Solids (2014) 256–284.
[45] B. Bourdin, J. Marigo, C. Maurini, P. Sicsic, Morphogenesis and propagation of complex cracks induced by thermal shocks, ArXiv e-prints, 1 (2013) 1–5.
[46] R. Davidge, T. Green, The strength of two-phase ceramic/glass materials, J. Mater. Sci. 3 (1968) 629–634.